Implementation and exploration of relative biological effectiveness in proton arc therapy

Stian Maurseth

Supervisors:
Kristian S. Ytre-Hauge

Helge Henjum

Lars Fredrik Fjæra

Master thesis in Medical Physics and Technology

Department of Physics and Technology

University of Bergen

March 2021

Acknowledgements

First of all, I would like to express my gratitude to my supervisors Kristian Smeland Ytre-Hauge, Helge Henjum and Lars Fredrik Fjæra. Your guidance and support has been invaluable to me.

Thank you, Kristian, for your guidance, feedback, and support over the past year, and for being available whenever I needed help. Thank you, Helge, for your guidance with the optimizer, proofreading my thesis and providing insightful feedback. Thank you, Lars Fredrik Fjæra, for helping me with constructing treatment plans in Eclipse, your guidance in the use of dose verification scripts and proofreading my thesis.

I would also like to express gratitude to flat mate and fellow student Jon Dyrkolbotn, as well as my fellow students: Annette Høisæter, Jon Asgeir Torsvik and Ingrid Mossige, whom I have been studying beside for the past 5 years. Thank you for your friendship and support, and for making the past five years a fun journey. A special thanks to Jon Dyrkolbotn for countless interesting discussions and

Lastly, I would like to thank my family for their encouragement and supportiveness. A special thanks go to my mother, Anne Karin Åkra, who helped spark my interest for logical reasoning, mathematics, and natural sciences at a young age.

Abstract

Purpose: The purpose of this study was to investigate the RBE in proton arc therapy and compare it to RBE in intensity modulated proton therapy plans. The use of RBE-models in treatment planning has the potential to reduce the physical dose needed for tumor control.

Methods: In this project the FLUKA MC code was used together with a prototype optimizer to calculate and optimize RBE-weighted dose distribution for IMPT and PAT plans. A treatment planning system was used to construct the plans used in this study. The treatment plan information was exported from the TPS and converted to a format that could be used for FLUKA simulations and the prototype optimizer. Mathematical description of two RBE models were included in the biological optimization of the plans, namely the McNamara model and the Rørvik unweighted model. The different treatment plans consisted of one IMPT plan and one PAT plan, for a water phantom case and a patient case. The dose distributions and RBE distributions for the different cases were compared. In addition, a PAT plan with lower maximum proton energy was made, to investigate the possibility and effect of placing the highest RBE and LET_d values inside the target volume.

Results: Across the water phantom and patient cases, the dose homogeneity and dose gradients were increased with the proton arc therapy plans. The calculation of physical dose distribution for the variable RBE-optimized plans, showed lower physical dose to the PTV compared to plans optimized with $RBE_{1.1}$ in all cases. For all cases the physical dose optimized with respect to the Rorvik unweighted model were lower than the physical dose optimized with respect to the McNamara model.

Conclusion: Based on the results in this study the use proton arc therapy has the potential to increase dose homogeneity and improve dose gradients compared to intensity modulated proton therapy. The application of variable RBE-models in treatment planning has the potential to lower the physical dose to the target volume, thereby preventing potential over-dosage of the tumor and surrounding healthy tissue. Significant differences were seen between the variable RBE-models. This gives rise to uncertainties, and therefore more research is needed before clinical implementation of variable RBE-models in treatment planning.

Contents

List of figures

List of tables

Glossary

CT	Computed Tomography
DSB	Double Strand Break
DVH	Dose Volume Histogram
GTV	Gross Target Volume
ICRU	International Commission for Radiation Units and Measurements
IMPT	Intensity Modulated Proton Therapy
IMRT	Intensity Modulated RadioTherapy
LET	Linear Energy Transfer
LET_d	Dose-averaged Linear Energy Transfer
LQ-model	Linear Quadratic Model
MC	Monte Carlo
MCN	McNamara RBE model
MRI	Magnetic Resonance Imaging
OAR	Organ At Risk
PAT	Proton Arc Therapy
PET	Positron Emission Tomography
PBS	Pencil Beam Scanning
PTV	Planning Target Volume
$RBE_{1.1}$	Dose calculated with a RBE of 1.1
RORU	Rørvik unweighted RBE model
ROI	Region Of Interest
SOBP	Spread-Out Bragg Peak
SSB	Single Strand Break
TPS	Treatment Planning System
VMAT	Volumetric Modulated Arc Therapy

1. Introduction

More than 34000 cancer cases were reported in Norway in 2019 [1]. Three of the main treatment modalities for cancer treatment are chemotherapy, surgery, and radiotherapy. About half of all cancer patients are eligible for radiotherapy at some stage during the course of their disease. The main goal of radiation therapy is to kill or sterilize tumor cells using ionizing radiation, while sparing the surrounding healthy tissue as much as possible.

External beam radiation therapy can be separated in to two main categories: Photon therapy and particle therapy. Photon therapy uses highly energetic photons to irradiate cells, while particle therapy uses massive particle such as protons or carbon ions. Massive particles are, in general, more effective at killing cells than photon radiation.

In recent years, the interest in proton beam therapy has spiked in Norway, as two proton centers are being built, one in Oslo and one in Bergen. Both centers plan to start treating patients with protons in 2024 [2].

1.1 A short history of radiation therapy

In November 1895 Wilhelm Röntgen discovered X-rays. Already in January 1896 X-rays were used to treat a patient with breast cancer, although the lack of knowledge of biological effect and physical mechanisms was extensive. Röntgen's discovery was followed by Becquerel's report on the phenomenon of radioactivity and Curie's discovery of radium. These discoveries sparked the start of the science of radiotherapy [3]. In the early 1900s the first high voltage X-ray tubes were made, and dose fractionation was proposed, as opposed to delivering all the dose at the same time. These discoveries, along with others, helped develop radiotherapy and led to better cure rates and better sparing of healthy tissue. In the 1950s the first electron linear accelerators became clinical available [4]. This made it possible to treat more deep-seated tumors, and it led to greater skin sparing and improved disease-control rates [3].

In 1946 Robert Wilson laid the groundwork for ion beam therapy with a paper proposing the use of protons and heavier ions for medical purposes [5]. The first clinical treatment using a proton beam was in Berkeley in 1954 [6]. In the following years, the use of protons for

radiotherapy became more widespread, and many proton therapy centers were built around the world. Treatments using heavier ions such as helium- and neon ions were first conducted in 1957 and 1975, respectively [7]. At the time treatment using protons and heavier ions was highly experimental, and it was done in physics laboratories [8]. The first hospital-based proton treatment facility was opened in 1990 in California USA [9]. The introduction of the CT scanner in the 1970s allowed treatment planning to shift from two- to three dimensions. In addition, CT-based systems allowed assessment of density variations in patient tissue. This increased the precision of dose planning, by reducing uncertainties tied to tissue heterogeneity. With CT-based planning and multileaf collimators (MLC), the latter was developed in the 1990s, the treatment could be done by sculpting the dose in three dimensions to cover the target volumes and avoid organs at risk (OAR) as much as possible.

In the 1990s and the 2000s new treatment methods, which further improved dose conformity and sparing of OARs, were introduced. The first commercial intensity modulated radiation therapy (IMRT) center was introduced in 1994 [10]. Followed by volumetric modulated arc therapy (VMAT) and adaptive radiotherapy (ART) in the 2000s. These new techniques made it possible to further customize treatment plans based on patients, locations, and tumor extents.

1.2 Proton therapy

One of the major advantages of using protons for radiation therapy, as compared to photons, is the differences in dose deposition, which is displayed in Figure 1.1. The dose distribution of photons is characterized by a short build up region, followed by an exponential dose falloff. This means that a considerable amount of healthy tissue will receive dose, especially for deep seated tumors. Because of the penetrating ability of photons, tissue behind the target will also receive dose. Comparably, the dose distribution of protons is characterized by a low dose region, followed by a dose increase and a sharp dose fall off. The high dose region of the dose deposition is called the Bragg peak, and

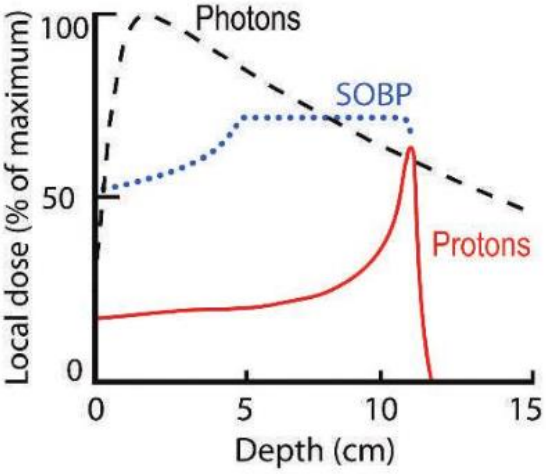

Figure 1.1: Depth dose curves for photons (dashed lines), protons (solid line) and a dotted line representing a spread out Bragg peak for protons [11].

it is located at the end of the proton range. Figure 1.1 also shows a spread-out Bragg peak (SOBP). The SOBP is made by using protons of many different energy layers. The sum of these protons dose curves results in a SOBP.

The VMAT technique for photon therapy was first described in 1993. It involves continuous rotation of the gantry, in one or more arcs, around the patient during treatment. This differs from IMRT where the radiation beam is switched off between gantry movements, between different beam angles. This technique increases dose confinement to the tumor and reduces toxicity to healthy tissue compared to other photon delivery techniques, such as IMRT [12]. Traditionally proton therapy has been delivered using a small number of beam angles, and varying the energy of the protons. This is referred to as intensity modulated proton therapy (IMPT). However, the benefits of VMAT compared to other photon delivery techniques has cause interest in the possibility of arc delivery techniques for proton therapy. In 2016 the first delivery efficient proton arc therapy (PAT) technique was introduced [13], and in 2019 the first prototype of proton arc treatment delivery was introduced [14]. Similarly to VMAT the treatment is delivered with continuous gantry rotation in one or several arcs around the patient. Proton arc therapy has the potential to increase healthy tissue sparing, reduce range uncertainty, improve dose conformity, and improve dose gradients, compared to VMAT and IMPT [15, 16]. Figure 1.2 shows an illustration of the IMPT and PAT delivery techniques.

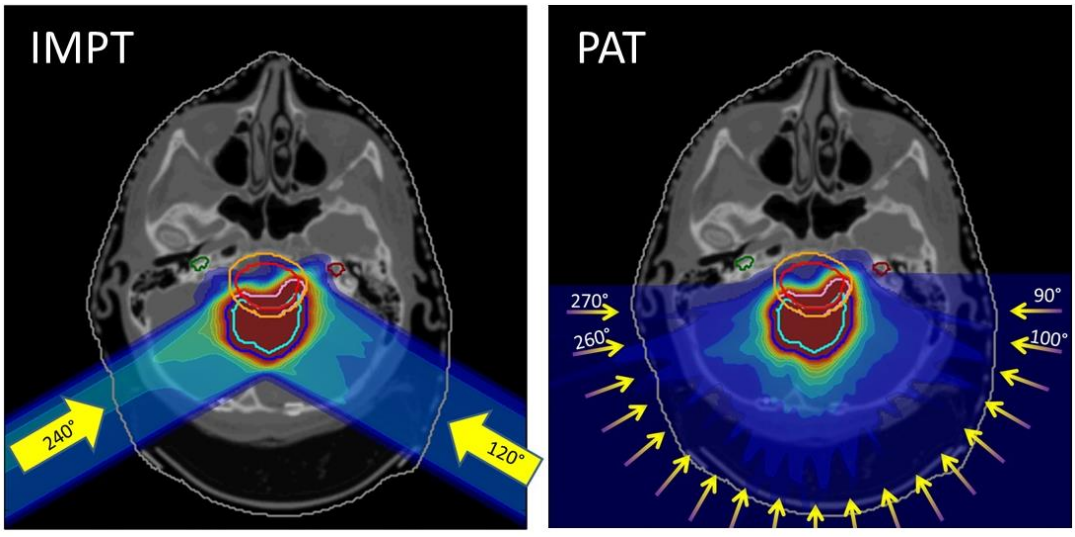

Figure 1.2:Illustration of dose distributions for the intensity modulated proton therapy (IMPT) and proton arc therapy (PAT) delivery techniques. The arrows represent different beam angles [17].

Proton therapy has in later years been established as an important modality, as it has several benefits compared to photon therapy. As mentioned, proton therapy offers better normal tissue sparing as well as very low dose deposition beyond the target volume. In addition, protons have an increased relative biological effectiveness (RBE) compared to photons. In clinical proton therapy a constant RBE of 1.1 is used, meaning that protons are ten percent more efficient at cell killing than photons. However, an increasing amount of experimental and clinical data show that RBE varies spatially within the patient, depending on factors such as tissue type, dose per treatment fraction and linear energy transfer (LET).

In addition to the different dose distributions between photons and protons, the biological effects, that is their ability to kill or sterilize cells, differs due to the differences in particle interactions between photons and protons. To describe this difference, the relative biological effectiveness (RBE) was introduced. The RBE is defined as the ratio between the dose delivered by a reference radiation (normally photons) and protons [18]. To account for the difference in RBE a constant RBE-factor of 1.1 is used in clinical proton therapy, meaning that protons are assumed to be 10% more effective at cell killing than photons [19]. However, an increasing amount of experimental and clinical data show that RBE varies spatially within the patient, depending on factors such as tissue type, dose per treatment fraction and ionization density.

1.3 Motivation

The use of a constant RBE of 1.1 is therefore view as an oversimplification, which in principle can lead to both over- and underdosage of the tumor, as well as higher dosage to surrounding normal tissue. Therefore, many variable RBE-models, based on experimental data, have been developed for proton therapy. These variable RBE-models generally predict higher RBE values than 1.1, especially at the distal area of the Bragg-peak. The use of RBE models in treatment planning and optimization could therefore increase the quality of treatment plans for proton therapy [20]. With the introduction of proton arc therapy, it is of interest to investigate the effects of variable RBE using this delivery technique.

The objective of this study is therefore to create a system for simulating proton arc therapy plans and examine the dose distributions to patients from this. Variable RBE-models will be

used to re-optimize treatment plans, calculate dose distributions from these plans, and compare the distributions to doses calculated with the clinically used RBE of 1.1, and to doses from conventional proton therapy plans.

2. The Physics of particle therapy

2.1 Proton interactions in matter

In radiotherapy protons have three main ways of interacting with matter: They are deflected by Coulomb scattering with nuclei, lose kinetic energy due to inelastic interactions with atomic electrons and undergo nuclear interactions with nuclei [21]. Protons are called heavy charged particles, as they have a large rest mass compared to the rest mass of electrons.

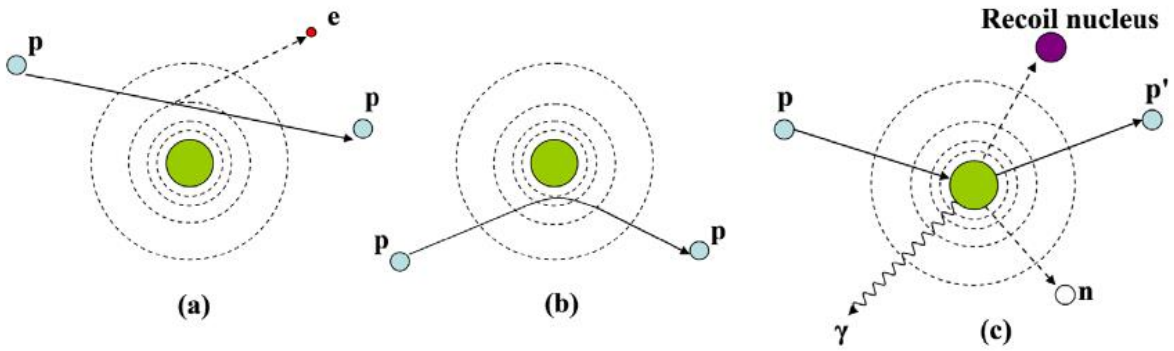

Figure 2.1: The three main interactions between protons and matter: (a) inelastic interactions with atomic electrons, (b) Coulomb-scattering with nuclei and (c) nuclear interactions [21].

2.1.1 Inelastic interactions with atomic electrons

The primary source of proton energy loss is through inelastic interactions with atomic electrons. Protons will interact with atomic electrons either by excitation or ionization of the electrons, and through these reactions the protons lose energy [22]. The mass of a proton is far greater than the mass of an electron, therefore the proton will not deviate significantly from its trajectory through interactions with electrons. Most of the secondary electrons will travel a short distance from the point of interaction, and they will ionize and deposit energy.

The Bethe-Bloch equation describes interactions between charged particles and atomic electrons [23]:

$$-\frac{dE}{dx} = 2\pi N_a r_e^2 m_e c^2 \rho \frac{Z}{A}\frac{z^2}{\beta^2}\left[ln\frac{2m_e v^2 \gamma W_{max}}{I^2} - 2\beta^2 - \delta - 2\frac{C}{Z}\right]. \quad (1)$$

Where dE is the energy loss over a small distance dx. The ratio dE/dx is called stopping power. The remaining variables are described in Table 2.1.

Table 2.1: Description of Bethe-Bloch equation variables.

Variable	Description	Variable	Description
N_a	Avogadro's number	A	Atomic mass of the absorber
r_e	Electron radius	z	Charge of the incident particle
m_e	Electron mass	β	Relativistic velocity
c	Speed of light	v	Speed of the incident particle
ρ	Density of the absorber	W_{max}	Maximum energy transfer from a single collision
Z	Atomic number of the absorber	δ	Density correction factor
γ	Lorentz-factor	I	Mean excitation potential
C	Shell correction factor		

The stopping power is inversely proportional to the proton velocity, which means that the protons will deposit most of their energy towards the end of their range. This results in a dose

distribution that increases with range, and towards the end of the proton path a Bragg peak, which will be explained in a later chapter.

2.1.2 Coulomb scattering

When protons pass close to nuclei, they are deflected due to the positive charged nuclei. Although each deflection is small, the sum of deflections is significant. Therefore, Coulomb scattering is accounted for in does calculations with treatment planning system [21]. The deflection is proportional to the incident particle's charge, and inversely proportional to the particle's velocity and atomic weight [24].

2.1.3 Inelastic nuclear interactions

In addition to the two interactions mentioned above, protons can also undergo nuclear interactions with nuclei. When the distance between a proton and a nucleus is sufficiently small, the proton can interact with the nucleus. In these reactions the nucleus may emit protons, neutrons, gamma rays or ion clusters. The emitted particle(s) contribute to the dose to the patient. And although most of the particles will not travel far from the beam track, neutrons might, as they do not have charge. This might cause dose to be deposited outside the planning volume [25].

2.2 Dosimetry and depth dose curves

2.2.1 Absorbed dose

The energy absorbed by matter from radiation is called absorbed dose, also referred to as physical dose. The definition of dose is defined as the energy deposited by ionizing radiation, dE, to a mass, dm [26]:

$$D = \frac{dE}{dm} \qquad (2)$$

The unit used for dose is Gray (Gy) in the SI system, and 1 Gy = 1 J/kg. It is important to note that the energy deposited by e.g. a proton beam is larger than the absorbed dose. As some of

the energy will be transferred to neutral secondary particles which can deposit dose outside of the volume of interest (eg. in the shielding of the treatment room) [27].

2.2.2 Spread-out Bragg Peak

Delivering a homogeneous dose to the whole target volume is important in clinical radiotherapy. ICRU recommends that the dose in the target volume should be no lower than 95% of the prescribe, and no higher than 107% [28]. With protons it is possible to produce a uniform dose distribution to the target using only one beam angle. This is done by modulating the proton energies to make a spread-out Bragg peak (SOBP). An example of this can be seen in Figure 2.2.

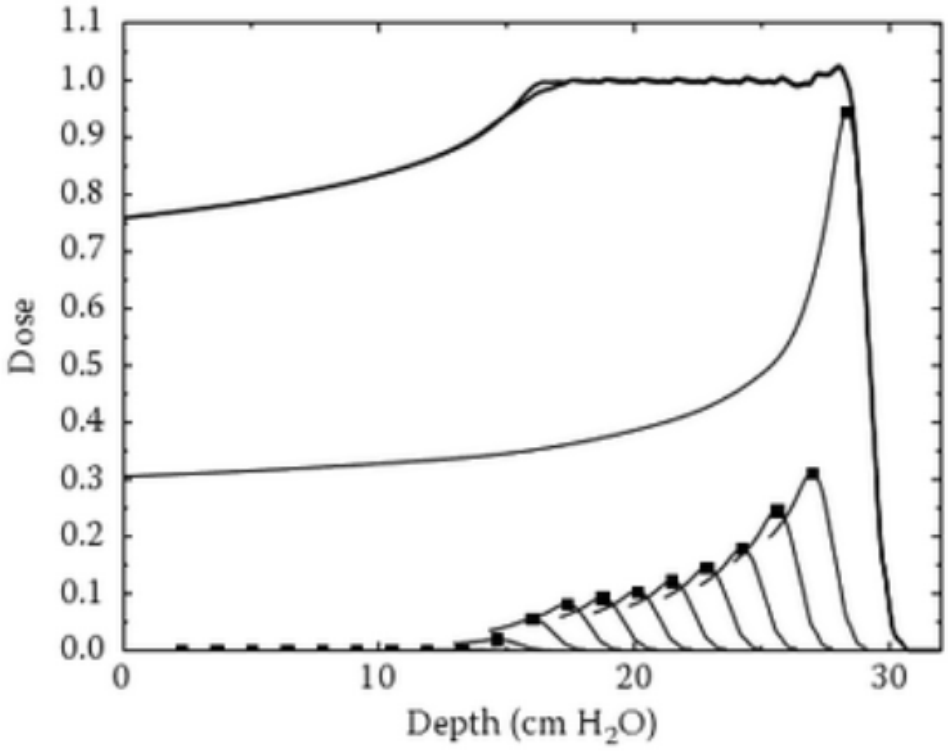

Figure 2.2: The use of different proton energies to create a spread-out Bragg peak [27].

2.3 Linear energy transfer

The Bethe-Bloch equation describes how much energy proton lose per unit length. However, there is a difference between this quantity and the energy absorbed by the medium. To describe this Zirkle introduced a quantity called linear energy transfer (LET) [29]. LET is defined as the energy transferred from the charge particle per unit length, to the biological material close to the particle track:

$$LET \equiv \frac{dE}{dx}\ , \left[\frac{keV}{\mu m}\right] \tag{3}$$

Higher LET values results in more effective cell killing as compared to lower LET values [30]. For protons, the LET increases with decreasing particle speed, which results in the protons being most effective at cell killing in the last part of their tracks. This gives protons an advantage in radiotherapy compared to photons, as they deposit most of their energy at the end of their path.

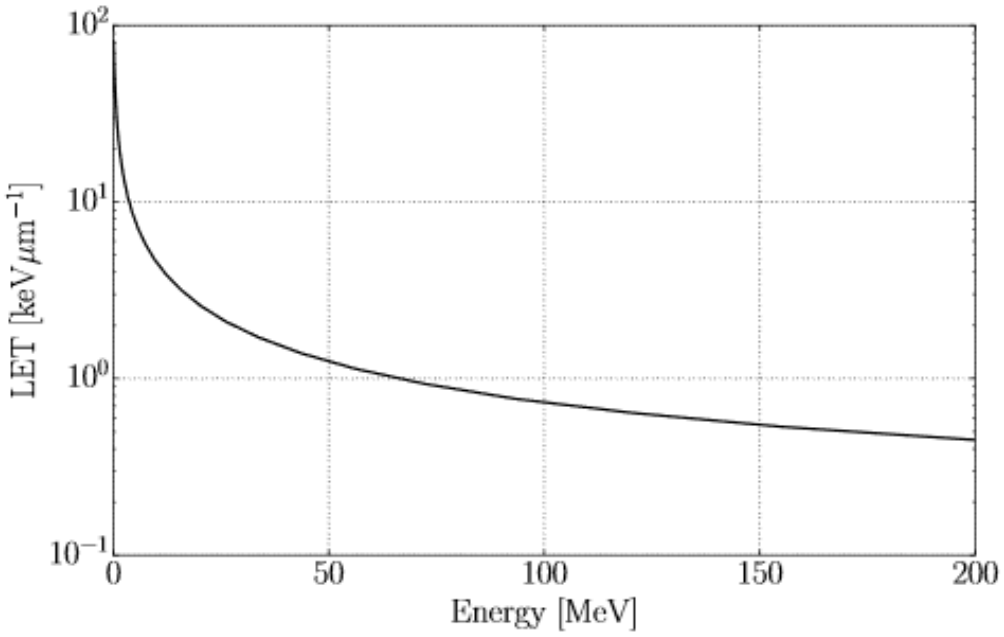

Figure 2.3: LET as a function of proton beam energy in water [31].

Most of the proton's energy is lost in the interactions described by the Bethe-Bloch formula, and deposited locally. However, a portion of the energy is converted to delta rays or bremsstrahlung. Bremsstrahlung is electromagnetic radiation produced by the deceleration of a charged particle when it is deflected by another charged particle. In these cases, the energy is deposited further away from the particle track. The LET with an energy cut-off to account for high energy delta rays is called the restricted LET and it is denoted LET_{Δ}. If no energy cut-off of delta rays is imposed, we get what is called the unrestricted LET:

$$LET_{\infty} \cong S_{el} \tag{4}$$

In this case the LET is equal to the electronic stopping power, S_{el}.

From the definition of LET, the dose-averaged LET (LET_d) can be derived. LET_d is a quantity that takes both dose and LET into consideration and it is therefore used when biological outcomes are studied [32]. When calculating LET_d the dose contribution of each individual energy deposition is used as the weighting factor:

$$LET_d(z) = \frac{\int_0^{\infty} S_{el}(E) D(E,z) dE}{\int_0^{\infty} D(E,z) dE} \tag{5}$$

Where S_{el} is the electronic stopping power of of a charged particle with kinetic energy E and D(E, z), is the absorbed dose contributed by the particle with kinetic energy E at a location z [32].

3. Radiobiology

3.1 Biological impact of ionising radiation

In radiotherapy the target in the cell is the DNA, as damage to the DNA is the main cause of biological effects from ionizing radiation [33]. Particles have two ways of interacting with biological matter: Through direct and indirect action. The first is when a particle ionizes atoms inside the target causing biological damage. This is most common for high-LET radiation such as low energy protons. The latter is when a particle ionizes other atoms close to the target, creating reactive molecules that cause biological damage.

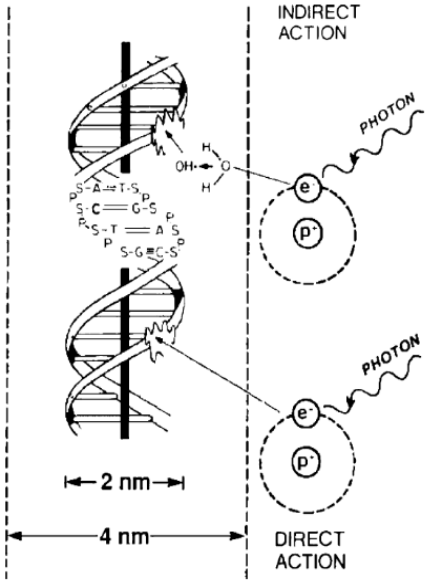

Figure 3.1: Illustration of indirect and direct action of radiation [32].

The most common damages to DNA in radiotherapy are single strand breaks (SSB) and double strand breaks (DSB). DSB are harder for the cell to repair because both strands of the DNA are damaged, and the cell cannot use one strand as a template to repair the other. Therefore, DSB are more effective than SSB at cell killing [33]. Higher LET leads to more damage being done through DSB. This implies that protons will have a higher biological effect compared to photons, as a larger percentage of the damage is done through DSB. Specifically, towards the end of their range, as proton LET values increases with decreasing proton energy.

3.2 The linear-quadratic model

The linear-quadratic (LQ) model is a commonly applied model that describes radiobiological effects and cell death. The model describes the surviving fraction (S) of cells after the cells have been irradiated by a dose (D). It is given by [18]:

$$S(D) = e^{-\alpha D - \beta D^2} \quad (6)$$

The parameters α and β are tissue specific parameters and determine the shape of the cell survival curve. The parameters can be correlated to single and double track events. At low doses there will be few double track events, and the α will dominate, while the β will dominate at higher doses as the amount of double track events increase [18]. The α/β ratio gives the deposited dose where the contribution from the linear part and the quadratic part of the LQ model is equal, i.e. when $\alpha D = \beta D^2$.

3.3 Relative biological effectiveness - RBE

The relative biological effectiveness (RBE) of protons is a measure the biological effect of protons compared to a reference radiation (X- or γ-rays)[19]. RBE is defined as [18]:

$$RBE = \frac{dose\ of\ reference\ radiation}{dose\ of\ test\ radiation} \quad (7)$$

In clinical proton therapy an RBE value of 1.1 is used ($RBE_{1.1}$). However, many studies have shown this to be incorrect [19], and have shown that the RBE depends on several factors such as LET, tissue type, charge, biological endpoint, and dose. In many instances the RBE is higher than 1.1, especially in the distal part of the SOBP, where the LET is high [19]. Proton treatment plans can be optimized by applying an RBE-weighted dose (D_{RBE}) to account for the difference in biological effectiveness between protons and photons. The RBE-weighted dose is also called the biological dose and it is defined as:

$$D_{RBE} = RBE * D \quad (8)$$

where D is the physical dose. In proton therapy the ICRU recommends using the RBE-weighted dose with units Gy(RBE) [34].

As mentioned, studies have shown that there is an increase in RBE in the distal part of the SOBP. This increase in RBE also causes a biological range extension and an increase in the effective beam range, that can be up to several millimeters (Figure 3.2).

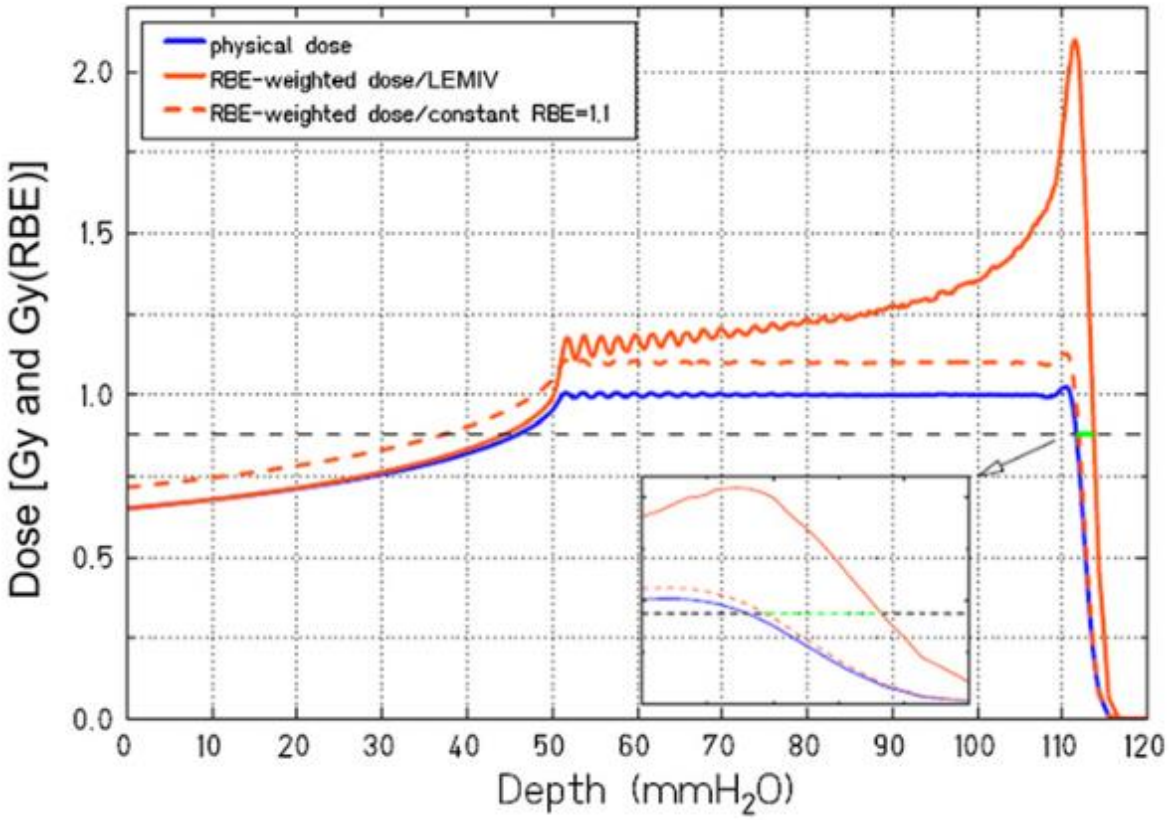

Figure 3.2: Illustration of the biological range extension. The blue line is the absorbed dose, the orange dashed line is the RBE-weighted dose using a constant RBE of 1.1 and the orange line is the RBE-weighted dose using a variable RBE model (LEMIV)[19].

As mentioned higher LET values results in more effective cell killing. Studies have shown that the RBE has a strong dependency on LET [19]. The relationship between RBE and LET can be seen in Figure 3.3. The figure also illustrates the relationship between RBE and dose levels, as the RBE decreases with less cell survival. Thus, the relationship between RBE and dose is inversely proportional. There is also a strong decrease in RBE for LET values higher than 100 KeV/µm. This is because of the overkill effect. For a cell to be killed enough energy has to be deposited into the DNA to produce a sufficient amount of DSB [18]. Very high LET values result in more energy being deposited into a cell than the energy needed to kill the cell. Thus, there is less likelihood per unit dose that other cells will be killed, which results in a decreased RBE.

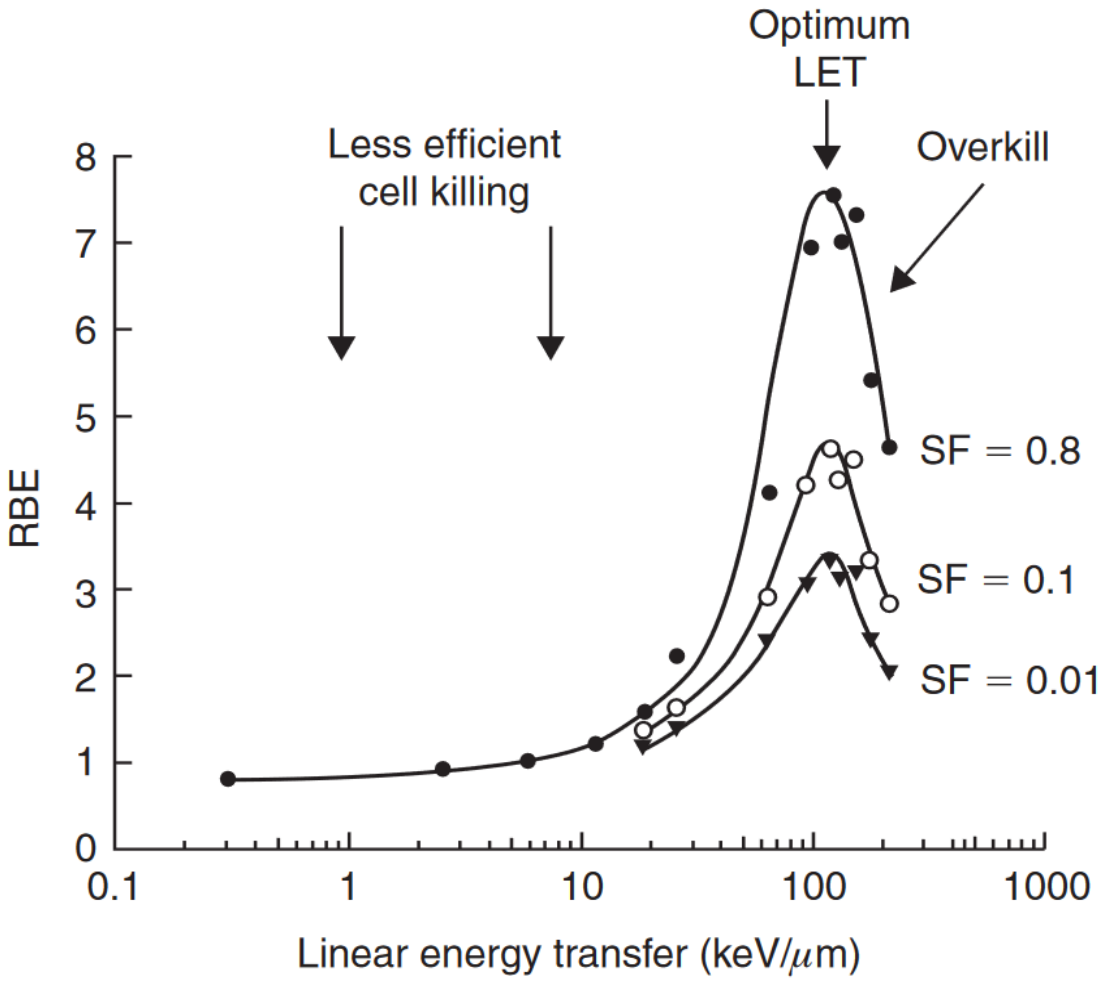

Figure 3.3: The relationship between LET and RBE for different surviving fraction levels: 0.8, 0.1 and 0.01 [18].

3.3.1 Biophysical RBE models

Many biophysical RBE models have been developed to predict the RBE in proton therapy. Nearly all models predict that RBE varies spatially with respect to variations in dose and LET, and the models therefore do not support the assumption of a constant RBE used clinically. Most RBE models are based on the LQ-model. From the LQ model (equation 6) the relationship between the photon and proton dose at the same survival can be described as follows:

$$S = e^{-\alpha D - \beta D^2} = e^{-\alpha_x D_x - \beta_x D_x^2} = S_x \quad (9)$$

Where D is the dose, and all variables with subscript x represent photon radiation while the others represent proton radiation. Solving this equation for the positive roots of D_x gives:

$$D_x = -\frac{1}{2}\left(\frac{\alpha}{\beta}\right)_x + \sqrt{\frac{1}{4}\left(\frac{\alpha}{\beta}\right)_x^2 + \frac{\alpha}{\alpha_x}\left(\frac{\alpha}{\beta}\right)_x D + \frac{\beta}{\beta_x}D^2} \quad (10)$$

Inserting the definition of the RBE (equation 7) into equation 10, gives the following expression for the RBE [35]:

$$RBE(D, \alpha, \alpha_x, \beta, \beta_x) = \frac{D_x}{D} = \frac{1}{2D}\left(\sqrt{\left(\frac{\alpha_x}{\beta_x}\right)^2 + 4D\left(\frac{\alpha_x}{\beta_x}\right)\left(\frac{\alpha}{\alpha_x}\right) + 4D^2\left(\frac{\beta}{\beta_x}\right)} - \frac{\alpha_x}{\beta_x}\right) \quad (11)$$

Further, expressions for the extreme RBE at low and high doses can be found by evaluating the upper and lower physical dose limits [35]:

$$\lim_{D\to 0} RBE = RBE_{max} = \frac{\alpha}{\alpha_x} \quad (12)$$

$$\lim_{D\to \infty} RBE = RBE_{min} = \sqrt{\frac{\beta}{\beta_x}} \quad (13)$$

Inserting equations 12 and 13 into equation 11 gives:

$$RBE\left(D, \left(\frac{\alpha}{\beta}\right)_x, RBE_{max}, RBE_{min}\right) = \frac{1}{2D}\left(\sqrt{\left(\frac{\alpha}{\beta}\right)_x^2 + 4D\left(\frac{\alpha_x}{\beta_x}\right)RBE_{max} + 4D^2 RBE_{min}^2} - \frac{\alpha_x}{\beta_x}\right) \quad (14)$$

All LQ-based RBE models can be formulated using equation however they differ in the definitions of RBE_{min} and RBE_{max} [36]. The RBE models used in this project are described in chapter 5.3.

4. Treatment planning and delivery in proton therapy

4.1 Treatment planning

The aim of treatment planning is to optimize the dose distribution to a target volume, while minimizing the dose to surrounding healthy tissue and organs at risk. Treatment planning is done by using simulation software known as treatment planning systems (TPS). The TPS simulates the treatment delivery and is used to calculate dose plans for patients.

In treatment planning there is a balance between risk and benefit. Planning aims to maximize the probability of curing the patient (tumor control probability) while minimizing the probability of negative side effects (normal tissue control probability) [27]. The tumor control probability depends on the dose delivered to the tumor, and the normal tissue control probability depends on dose delivered to normal tissue. The possibility of achieving good tumor control is illustrated in Figure 4.1, and is often referred to as the therapeutic window [37].

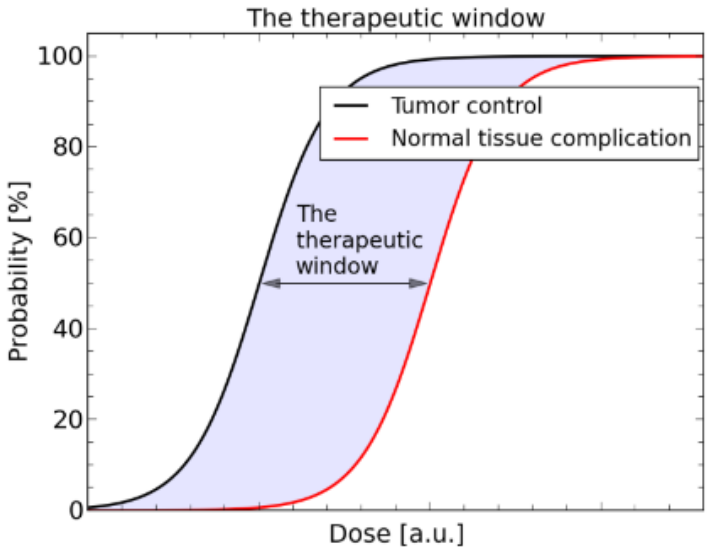

Figure 4.1: Illustration of dose response curves for tumor control probability and normal tissue control probability. The gap between the two curves represent the potential for curing the patient while keeping the probability of side effects low [24].

4.1.1 Image acquisition

The first step in the treatment planning process is to acquire images of the patient that can be used for planning in the TPS. The most common medical imaging modalities are computed tomography (CT), magnetic resonance imaging (MRI), positron emission tomography (PET) and ultrasound (US). Although all these modalities have advantages and disadvantages, CT is most used for radiotherapy as it can acquire tissue density information [38].

4.1.2 Anatomical volumes

The next step in the treatment planning process is importing the CT images into a TPS and delineating volumes of interest. Medical doctors and physicist use the acquired images to define volumes inside the patient, such as the target volume and organs at risk (OAR) [39]. Two important volumes defined in this process is the gross target volume (GTV) and the clinical target volume (CTV). The GTV is defined by the visible tumor, while the CTV takes invisible tumor growth into account. Then patient movement uncertainties and dose delivery uncertainties is accounted for, to delineate a planning target volume (PTV) [27]. The OARs are typically normal tissues or organs with a high radiation sensitivity. Therefore, they are delineated, as they significantly influence the dose planning prosses. Similarly, as for the PTV a planning organ at risk volume is delineated (PRV), to assure a high probability of adequate sparing of the OARs.

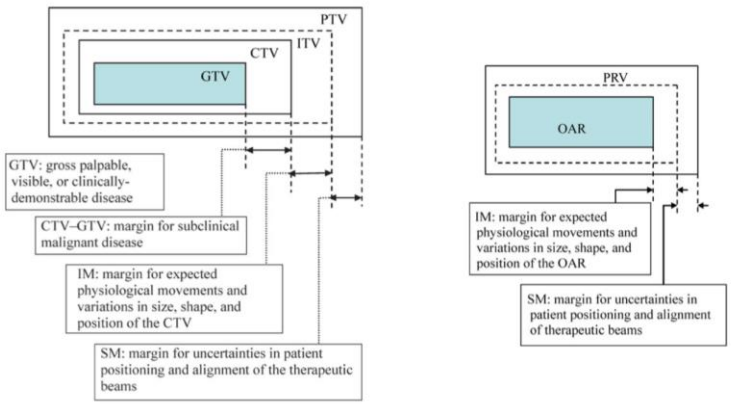

Figure 4.2: Illustration of target volumes, OARs and safety margins as defined by ICRU [34].

4.1.3 Dose planning

After all relevant volumes have been delineated the dose planning process starts. Then planning aims are prescribed, i.e. dose requirements for the PTV and normal tissue constraints for the OARs. The planning aims are based on thorough evaluation of the patient as well as diagnostic studies and ontological concepts. The treatment planner uses the planning aims to find a basis for an acceptable compromise between the dose to the target and the OARs [27].

4.1.4 Plan optimization

In intensity modulated proton therapy (IMPT) inverse planning is typically used. With pencil beam scanning each pencil beam can be steered by magnets to conform dose in the transverse plane (see Section 4.2.1). This type of conformation is also achievable with photons through IMRT or VMAT. However, the Bragg peak gives an additional degree of freedom for protons because modulation along the beam axis is possible. With pencil beam scanning each beam is weighted and optimized separately [34]. The optimization process consists of iteratively generating and assessing many plans and choosing the best one. This is achieved by giving a computer constraints and objectives. Constraints cannot be broken, while objective are given weights relative to each other, and in some cases small violations of the objectives can be allowed. After the computer has calculated a plan, the plan is assessed by a treatment planner, who makes sure the results are satisfactory. If they are not the constraints and objectives can be changed, and the plan can be reoptimized.

4.1.5 Plan assesment

Several different methods are used to evaluate treatment plans. Dose levels are displayed both on 2D CT images of the patients, either as a dose color wash or isodose lines and dose volume histograms (DVH) are made. These graphical displays are compared to the constraints and objectives given in the optimization process. Although the CT images give an impression of how the dose is distributed, it can be difficult to assess a plan in terms of dose delivered to different clinical volumes from such images alone. Therefore, DVHs are used in conjunction with the images. DVHs provide a better way to compare plans than dose images, although the spatial information is lost in the DVHs. The loss of spatial information can be compensated for by looking at both the DVHs and the CT dose images.

4.1.6 Uncertainties

There are a lot of factors that contribute to the uncertainties of dose delivery in proton therapy. Firstly, there are uncertainties tied to patient alignment and setup. External markings on the patient are used to realign the patient for treatment after imaging. The imaging should therefore be done in the same patient position as the treatment delivery. In addition, patients are often immobilized to reduce the uncertainty tied to patient movement. Tissue heterogeneities and CT conversion uncertainties contribute to range uncertainty. Because of the many factors contributing to treatment delivery uncertainties, regulatory bodies suggests an aim that the delivered dose should be within 2.5% of the prescribed dose [8].

4.2 Treatment delivery

4.2.1 Beam delivery techniques

In proton therapy there are two main beam delivery techniques to deliver a homogeneous dose to the target, passive scattering, and active scattering. The latter is also called spot-scanning proton therapy, and it makes use of pencil beam scattering (PBS). PBS have advantages over passive scattering when it comes to optimizing dose to target volumes, and it is therefore implemented in all new proton therapy centers. With PBS dipole magnets are used to steer the proton beam in the horizontal and vertical direction. In addition, the energy of the beam is changed to irradiate different layers of the target (see Figure 4.3).

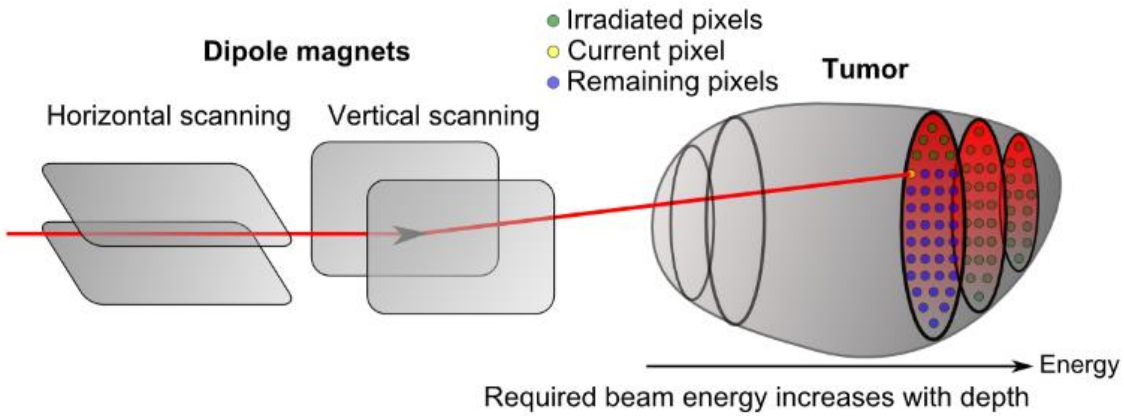

Figure 4.3: Illustration of the pencil beam scanning technique [24].

4.3 Proton arc therapy

In radiation therapy and arc refers to a gantry rotation, either continuous or discontinuous, around the isocenter. IMPT treatments are usually delivered using a small number of beam angles (1-5), and the beam is turned off while the gantry moves between the different angles. However, the concept of proton arc therapy (PAT) was first introduced in 1997 [40], to combine the unique dose deposition curve of protons and the benefits of rotating beams. PAT is not practical for clinical application with passive scattering, due to the difficulty of changing beam specific compensators and range modulator during gantry rotation. However, the increasing adoption of the spot scanning technique makes PAT technically viable.

Different delivery methods have been proposed for spot-scanning proton arc therapy, like multiple static fields [16], distal edge tracking [41], and single energy modulation [42]. The multiple static fields delivery method consists the use of many static fields and beam angles for treatment delivery, meaning that the beam is turned off during gantry rotation. In distal edge tracking, all Bragg peaks are placed at the edge of the target volume. Single energy modulation is based on using one or two energy layers for all proton beams. However, all these methods either cannot perform continuous rotation-delivery or fail to utilize the freedoms in the spot-scanning technique. Research is still being done on the topic of developing efficient delivery methods for PAT, in order to implement the technique clinically.

The concept of proton arc therapy is becoming clinically available, with a recent demonstration of deliverability of a spot-scanning proton arc plan within clinical requirements. [14]. The dosimetric benefits of proton arc therapy has been demonstrated in several studies. PAT has been shown to reduce skin dose, reduce integral dose, increase plan robustness, and increase normal tissue sparing for both extra-, and intra-cranial tumor [43-45]. Studies also demonstrate reduced treatment times with PAT compared to both VMAT and IMPT [14, 43].

4.4 Monte Carlo Simulations

Monte Carlo simulations is widely accepted to be the best way to provide accurate dose calculations [46]. By randomly sampling the possible outcomes of different particle interactions and physical processes from probability distributions, the Monte Carlo method

can simulate real world particles on a particle-by-particle basis. The simulations also take tissue heterogeneities into account, by using information about material properties, such as atomic composition and electron density. Each interaction that occurs in the simulation determines the next step in the simulation. If secondary particles are created in interactions, they are tracked as well. The precision of the Monte Carlo simulations is dependent on the number of event (N) in the simulation, and the uncertainty is proportional to $1/\sqrt{N}$, where N is the number of particles.

4.5 DICOM files

The DICOM file format is the standard format for storing information in medical imaging. The DICOM files contain the information needed to execute simulations of radiotherapy, such as images of the patient, coordinates of regions of interest, particle energies, gantry angles, etc. The DICOM format also makes the exchange of data between different software simpler.

The DICOM files consist of four different file types: DICOM CT images, DICOM RT structure set, DICOM RT plan and DICOM RT dose. The CT images are stored as multiple files, one for each planar slice of the patient. As mentioned, the CT images contain information about density, as well as information about pixel size and patient orientation. The RT structure set contains information about the different ROIs, such as the PTV, CTV, and OARs. The structure set defines the coordinates of all the structure, and this is useful for visual dose displays, and needed to calculate DVHs. The RT plan file contains geometric and dosimetric data, and specifies beam properties, such as beam angles, beam modifiers and isocenter position. The RT dose file contains the dose data calculated in the TPS, as well as information about scoring regions and the sizes of scoring grids.

5. Materials and methods

This chapter will describe the process of simulating and re-optimizing treatment plans. An overview of the process can be seen in Figure 5.1. Descriptions of the scripts used in the process can be found in Appendix A. The first step of the process was to generate treatment plans using the Eclipse treatment planning system (Varian Medical Systems, Palo Alto, California US). In Eclipse the plans were optimized with a constant RBE of 1.1. The plans were exported and the information from the treatment plan was modified into a format that could be used as input for FLUKA. Then MC simulations were run in FLUKA, and the output of the simulation was used in conjunction with other files to run the optimizer. The optimizer modifies the weightings of each individual pencil beam with respect to variable RBE-models chosen by the user. Finally, a FLUKA simulation was run with the RBE-optimized plans to generate the optimized dose distributions.

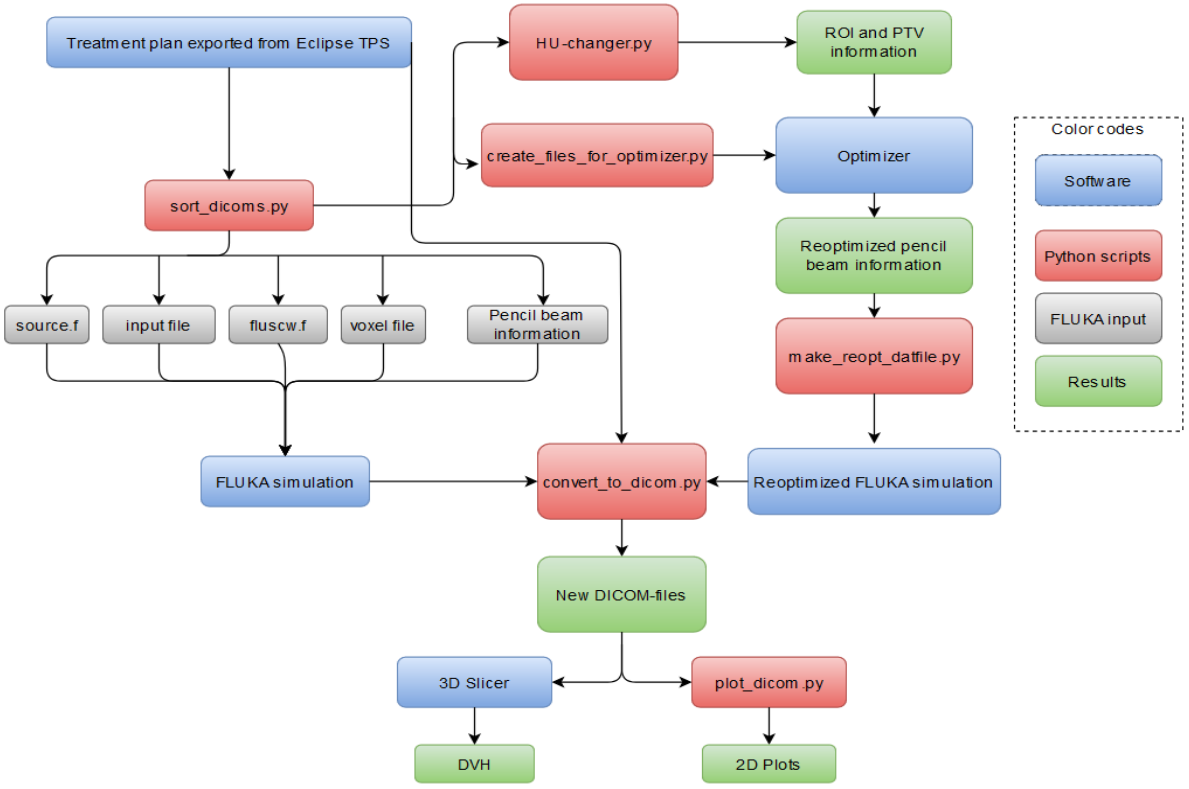

Figure 5.1: Flowchart showing the steps of the simulation and re-optimalization process. Explanation of the different steps can be found in Appendix A.

5.1 Software

5.1.1 Eclipse treatment planning system

The Varian Eclipse TPS was used in this project to make treatment plans for a water phantom case and a patient case. It is also used at Haukeland University Hospital. Eclipse lets the user create plans for various treatment modalities, including proton beam therapy. Plans exported from Eclipse are in the DICOM (Digital Imaging and Communications in Medicine) format.

5.1.2 FLUKA

In this project the FLUKA MC code[47-49] was used together with FLAIR [50](FLUKA advanced interface). The subroutines used with FLUKA in this project were the source and the fluscw routines. The source routine reads pencil beam information and converts the information so it can be understood by FLUKA. The fluscw routine enables scoring of biological parameters by choice. As the Eclipse TPS calculate dose to water, the same was done in FLUKA, to enable direct comparisons of the delivered dose. As dose is given by $fluence * \frac{LET}{\rho}$, where ρ is the density of the material, this is set to the density of water (1g/cm^3). The fluscw routine also includes a table containing α and β values, which is multiplied by $fluence * LET$ to calculate biological variables needed for biological dose calculations.

VOXEL files, that define the geometry of the simulations, are made in FLAIR. This is done by converting the Hounsfield units from CT images, imported in the DICOM file format, into material densities and material compositions [51]. After the plan information, the source and fluscw routines and the VOXEL file have been imported or made in FLUKA, simulations can be run. Then information about the simulations, such as dose data can be exported and further processed. In this project the data was processed and examined using several python scripts (described in Appendix A) as well as using the software program 3D Slicer (see 5.1.4).

The statistical uncertainty of FLUKA simulations is dependent on the number of primaries used in the simulations. The statistical errors of MC simulations are dependent on $\frac{1}{\sqrt{N}}$.

Therefore, the simulations in this project were run with 5000 primaries per beamspot to ensure reasonably low uncertainties.

5.1.3 Optimizer

An optimizer was used in this project to optimize the treatment plans with respect to biological dose with variable RBE-models. The models used in this project are described in chapter 5.3. The optimizer uses information about the pencil beams, physical dose, the biological variable α and β, and a voxel file to calculate new weightings for each individual pencil beam, with respect to the chosen biological model. The cell-line for the biological models is manually imported into the optimizer. In this project an $\alpha\beta - ratio$ of 2Gy was chosen for all treatment plans.

5.1.4 3D Slicer

3D Slicer is a software made for medical imaging and informatics. Slicer reads DICOM files and can be used to create 1D, 2D and 3D plots of dose distributions. In this project Slicer was used, together with the extension SlicerRT, for DVH calculations.

5.2 Treatment plans

Treatment plans were first made for a cylindrical PTV in water, before proceeding to patient plans. All treatment plans and the water phantom were made in the Eclipse TPS.

5.2.1 Cylindrical PTV in water

The water phantom geometry consists of a cylindrical water phantom with radius 10cm and height 10cm, and a PTV with radius 2 cm and height 10cm, placed in the center of the phantom. A cylindrical phantom was chosen because of its symmetrical properties. An illustration of the water phantom can be seen in Figure 5.2.

For this project three different treatment plans were made for the water phantom. For all water phantom plans the PTV was prescribed a homogeneous dose of 2Gy(RBE) The first plan consists of two opposing proton fields, as seen in Figure 5.2.

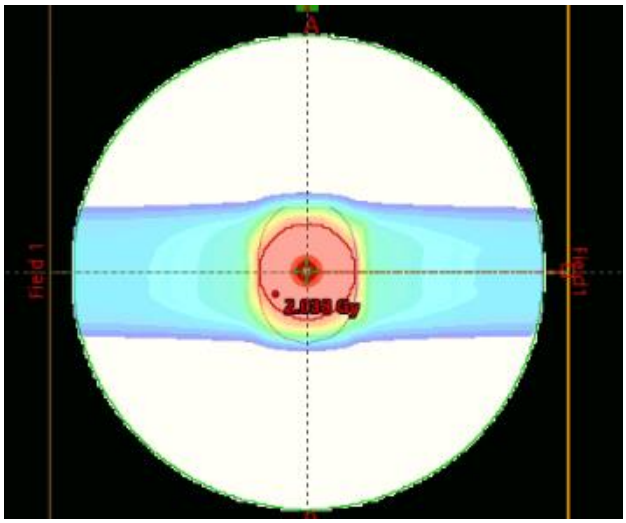

Figure 5.2: Illustration of the water phantom. The green outline marks then entire phantom, and the red outline marks the PTV.

The second plan is a 360^{O} arc plan consisting of 64 fields, equally spread around the phantom.

The third plan is also a 360^{O} arc plan consisting of 64 fields, however in this plan the highest energy layers of each beam have been removed. This was done as an attempt to shift the highest RBE-values from outside to inside the PTV, as the highest RBE-values can be found at the end of the proton range generally outside the PTV in clinical proton treatment plans. For all water phantom plans the PTV was prescribed a homogeneous dose of 2Gy(RBE).

5.2.2 Patient plans

Two patient plans are included in this study. The patient case is a brain germinoma case, where two separate plans were created and simulated. The first plan consists of two opposite proton fields and can be seen in Figure 5.3. This plan was made as a comparison to the proton arc treatment plan.

The proton arc plan was made with two opposite 120^{O} arcs, and the arc was constructed by having 8 fields on each side of the patient at different angles. The arc plan can be seen in Figure 5.4. Both plans were optimized to give a homogeneous dose of 54Gy(RBE) to the PTV, with 1.8Gy(RBE) per fraction, meaning 30 total fractions.

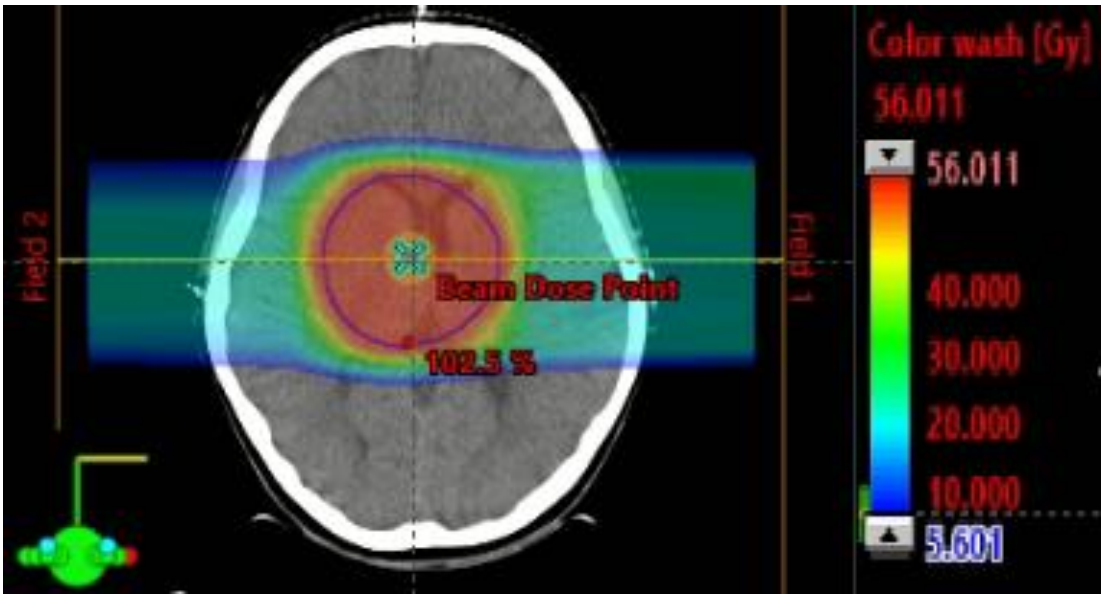

Figure 5.3: Patient plan with two opposite fields made in Eclipse TPS, where the figure was taken from. The purple outline represents the PTV.

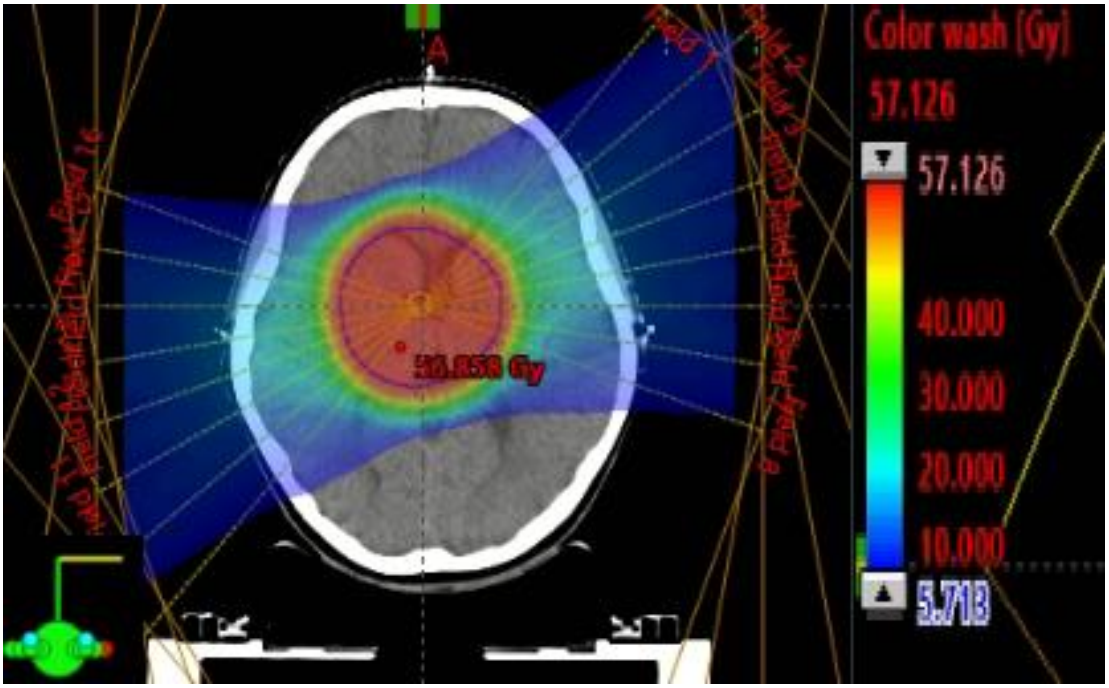

Figure 5.4: Patient proton arc plan. The plan was made in Eclipse TPS. The purple outline represents the PTV.

5.3 RBE-models

In this project, two variable RBE-models were used: The model by McNamara et al. (MCN)[52], and the unweighted model by Rørvik et al (RORU)[36]. Both models use the LET_d and $\left(\frac{\alpha}{\beta}\right)_x$ for photons as input parameters.

The MCN model assumes that the RBE_{max} have a linear dependence on both the LET_d and $\left(\frac{\alpha}{\beta}\right)_x$, while the RBE_{min} has a linear dependence on LET_d and a dependence on $\sqrt{\left(\frac{\alpha}{\beta}\right)_x}$. These gives the following equations:

$$RBE_{max}\left[\left(\frac{\alpha}{\beta}\right)_x, LET_d\right] = p_0 + \frac{p_1}{\left(\frac{\alpha}{\beta}\right)_x} LET_d,$$

$$RBE_{min}\left[\left(\frac{\alpha}{\beta}\right)_x, LET_d\right] = p_2 + p_3\sqrt{\left(\frac{\alpha}{\beta}\right)_x} LET_d \qquad (15)$$

Where p_{0-3} are fit parameters for the model. MCN then uses Matlab to fit the model to experimental data, and end up with the following equations:

$$RBE_{max}\left[\left(\frac{\alpha}{\beta}\right)_x, LET_d\right] = 0.999064 + \frac{0.35605}{\left(\frac{\alpha}{\beta}\right)_x} LET_d$$

$$RBE_{min}\left[\left(\frac{\alpha}{\beta}\right)_x, LET_d\right] = 1.1012 - 0.0038703\sqrt{\left(\frac{\alpha}{\beta}\right)_x} LET_d \qquad (16)$$

The RORU model assumes a linear dependency between the RBE and LET. In addition, the RORU model assumes that $RBE_{min} = 1$, due to other published models having found only small deviations of the RBE_{min} from 1 for all $\left(\frac{\alpha}{\beta}\right)_x$ and LET values [36]. The RBE_{max} for the RORU model is described by the following equation:

$$RBE_{max}\left[\left(\frac{\alpha}{\beta}\right)_x, LET_d\right] = 1 + \frac{0.645}{\left(\frac{\alpha}{\beta}\right)_x} LET_d \qquad (17)$$

6. Results

In this section the results from the FLUKA simulations will be displayed. This includes dose distributions, LETd and RBE-weigthed doses and RBE-distributions, for each phantom and patient plan. In addition, comparisons between the dose distributions for $RBE_{1.1}$ and for the two models are displayed, as well as DVHs and dose metrics for each plan. Figures and tables displaying information about the results are placed together for the water phantom 2 fields case and water phantom arc case, as well as after the patient 2 fields case and patient arc case, to make comparing the results of IMPT and proton arc therapy easier.

6.1 Water phantom

6.1.1 Cylindrical PTV in water - 2 opposing fields

Figure 6.1 shows the dose distribution on a plane through the middle of the PTV (marked as a red circle), for $RBE_{1.1}$ as well as for the two variable RBE models used, McNamara and Rorvik. The plot shows that the dose-distribution is relatively homogenous for all models. However, the DVH in Figure 6.7 and the dose metrics in

Table 6.1 show that the dose for both variable models were less homogenous than for $RBE_{1.1}$. Although, the variable models predict less homogenous dose to the PTV, the mean doses predicted by $RBE_{1.1}$, MCN and RORU (2.01Gy(RBE), 2.03Gy(RBE) and 2.03Gy(RBE) respectively) are similar for all models.

The DVH in Figure 6.7 also displays the corresponding physical doses for each biological model. The mean physical doses predicted for $RBE_{1.1}$, MCN and RORU were 1.83 Gy(RBE), 1.64 Gy(RBE) and 1.50 Gy (RBE) respectively. Meaning that both variable models predict lower physical doses than $RBE_{1.1.}$

From the dose metrics in Table 6.1it can be seen that the absolute and relative difference between the mean dose (column 2) and $D_{2\%}$ (column 4) is higher for both variable RBE models

than for $RBE_{1.1}$. Meaning that the variable models predict higher dose to be delivered to a small part of the PTV compared to the mean dose predicted.

Figure 6.3 shows RBE distributions for the variable models, Figure 6.5 shows an LET_d distribution and Table 6.2 shows RBE metrics for the PTV for each variable model. The figure shows that both models predict RBE values above 1.1 inside the PTV. The mean RBE predicted inside the PTV by MCN and RORU were 1.23 and 1.35 respectively. The figures also show that high LET values correspond with high RBE values, and that both the highest RBE and LET values are found outside the PTV.

6.1.2 Cylindrical PTV in water - 360^O arc plan

Figure 6.2 shows the biological dose distributions for the 360^O arc treatment plan. The figure shows that the PTV receives a reasonably homogenous dose of 2.0Gy(RBE) for all RBE models, and this is supported by the DVHs in Figure 6.8. This shows this shows that the optimizer is able to produce a homogeneous dose, also when applying RBE-models and 360^O arcs.

From the dose metrics in Table 6.1, as well as the DVH in Figure 6.8, it can be seen that the dose profiles for the three models are very similar. Both $D_{95\%}$ and $D_{2\%}$ are within 0.04Gy of the mean dose for each separate model. The dose metrics show that the mean doses to the PTV predicted by $RBE_{1.1}$, MCN and RORU were 2.01Gy(RBE), 2.01Gy(RBE) and 1.99Gy(RBE) respectively. The DVH also display physical doses corresponding to each biological model. The physical doses corresponding to MCN and RORU are lower than the physical dose corresponding to $RBE_{1.1}$. Physical doses predicted by $RBE_{1.1}$, MCN and RORU are 1.83Gy(RBE), 1.63Gy(RBE) and 1.45Gy(RBE), respectively. Illustrating hot the use of RBE models reduces the physical dose deposition in this case.

Figure 6.4 shows RBE distributions for the McNamara and Rorvik models, Figure 6.6 shows an LET_d distribution and Table 6.2 shows RBE metrics for the PTV for each model. Both the MCN and RORU models predict higher RBE-values for the entire PTV than $RBE_{1.1}$. The mean RBE in the PTV for MCN and RORU were 1.23 and 1.35, respectively. The figures also show that high LET values correspond with high RBE values, and that both the highest RBE and LET values are found outside the PTV. Overall, the RORU model predicts slightly higher

RBE values than the MCN model. This is in agreement with previous work done by Rørvik, et al. [53].

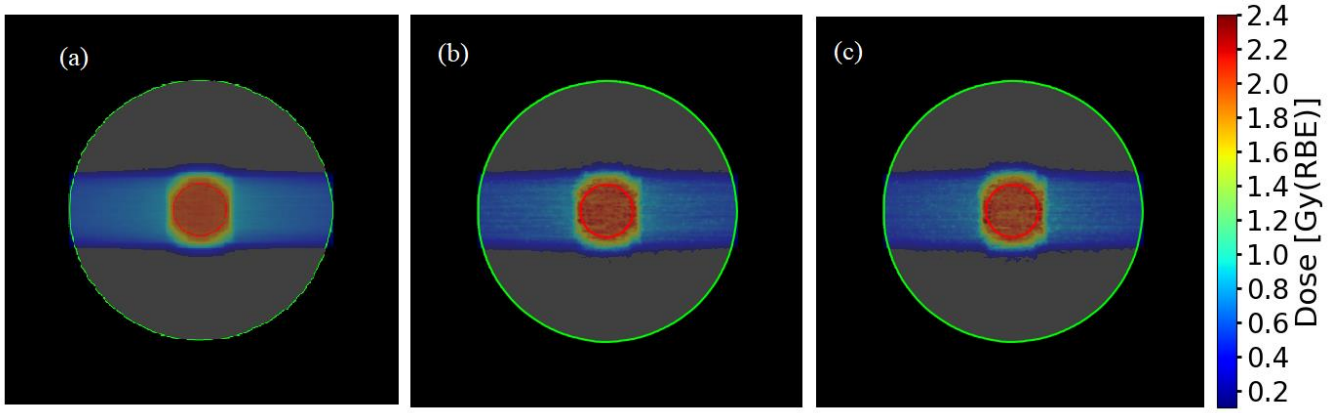

Figure 6.1: RBE weighted dose distributions for the water phantom case with two opposing fields, for (a) $RBE_{1.1}$ and for the biological models (b) MCN and (c) RORU in a plane through the center of the PTV. The PTV is marked with a red outline. The prescribed dose to the PTV is 2.0 Gy.

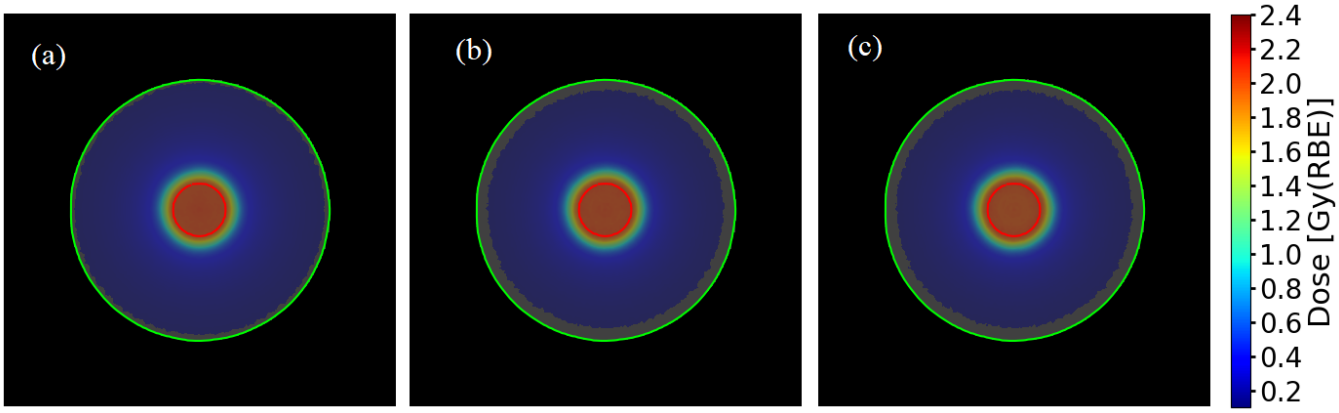

Figure 6.2: RBE weighted dose distributions for the water phantom 360^{O} arc case, for (a) $RBE_{1.1}$ (b) MCN and (c) RORU in a plane through the center of the PTV. The PTV is marked with a red outline. The prescribed dose to the PTV is 2.0Gy.

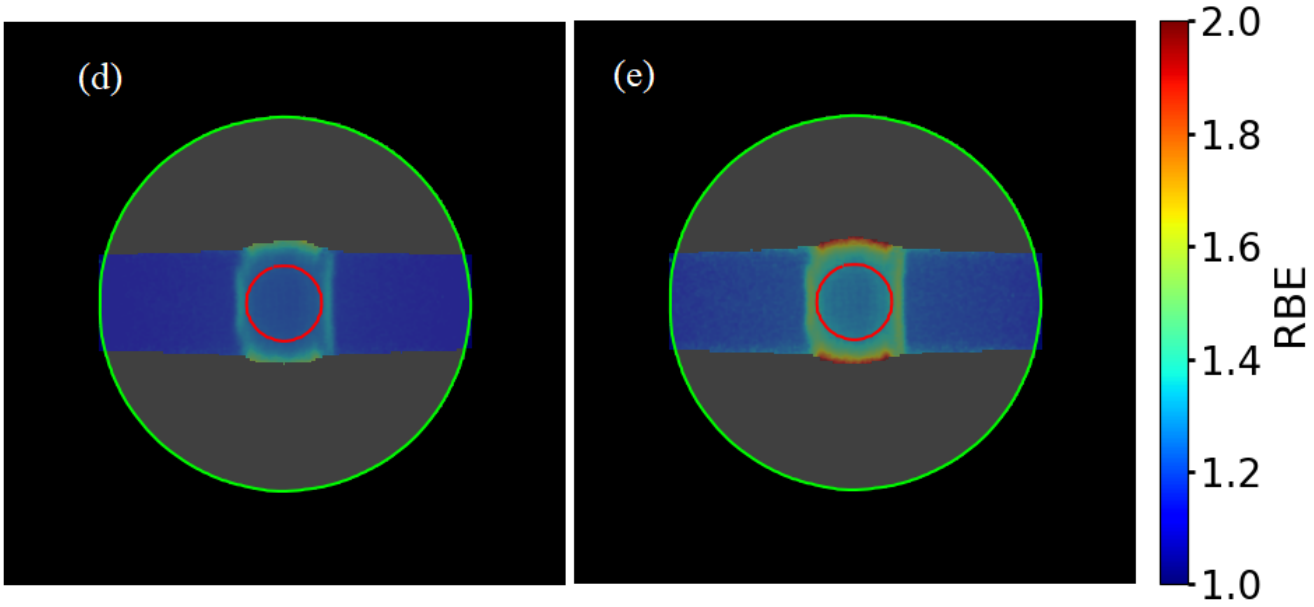

Figure 6.3: RBE distributions for the water phantom case with two opposing fields, for (d) MCN and (e) RORU.. The dose cutoff was set to 0.2 Gy.

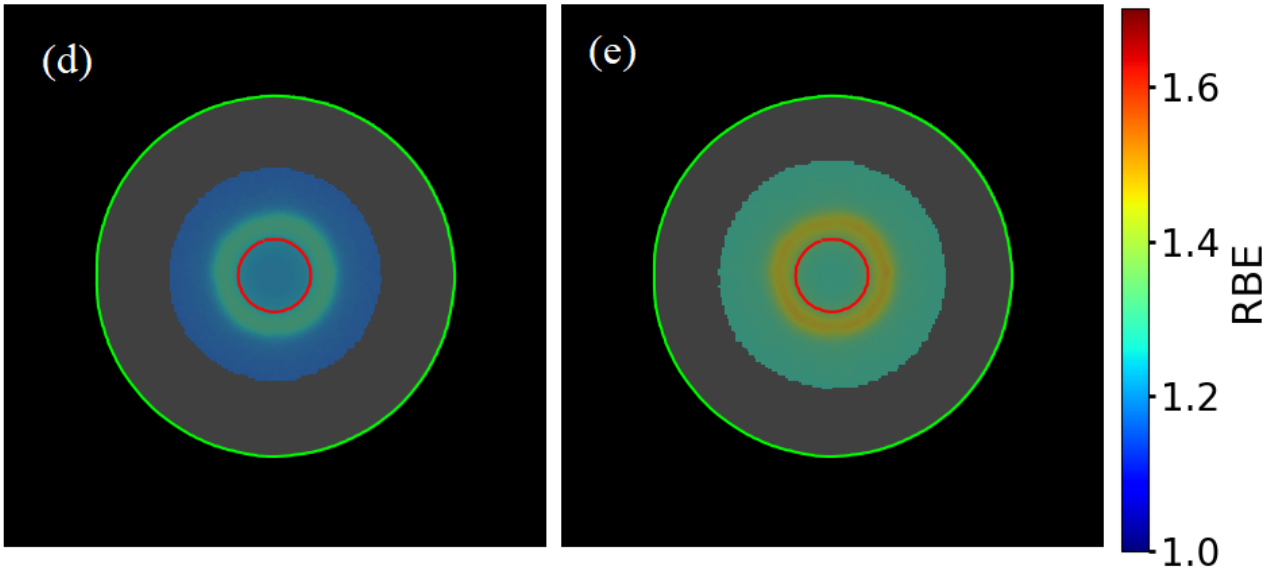

Figure 6.4: RBE distribution for the water phantom 360^{O} arc case, for (d) MCN and (e) RORU and LET_d distribution (f). The dose cutoff was set to 0.2 Gy

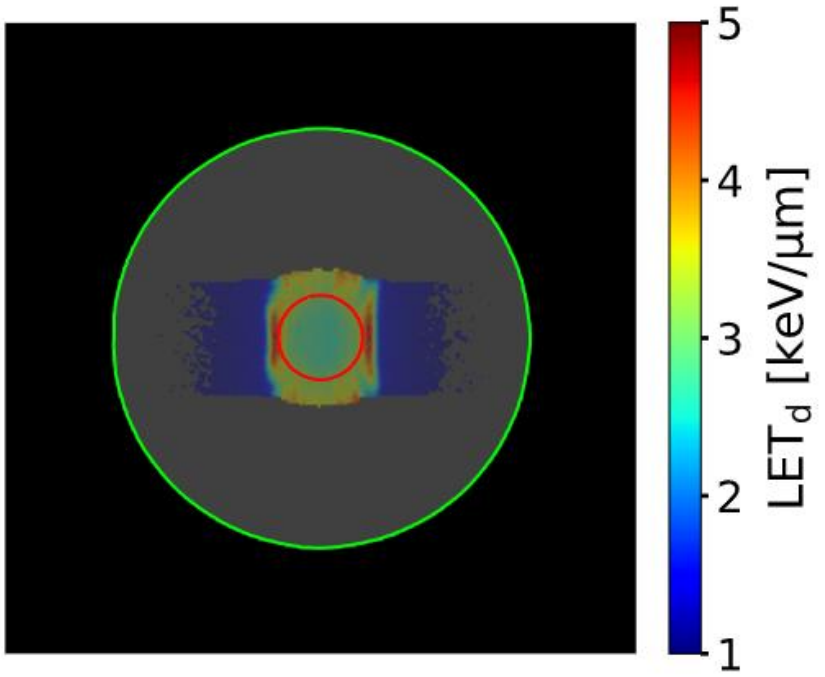

Figure 6.5: LET_d distribution for the water phantom case with two opposing fields. The dose cutoff was set to 0.2Gy.

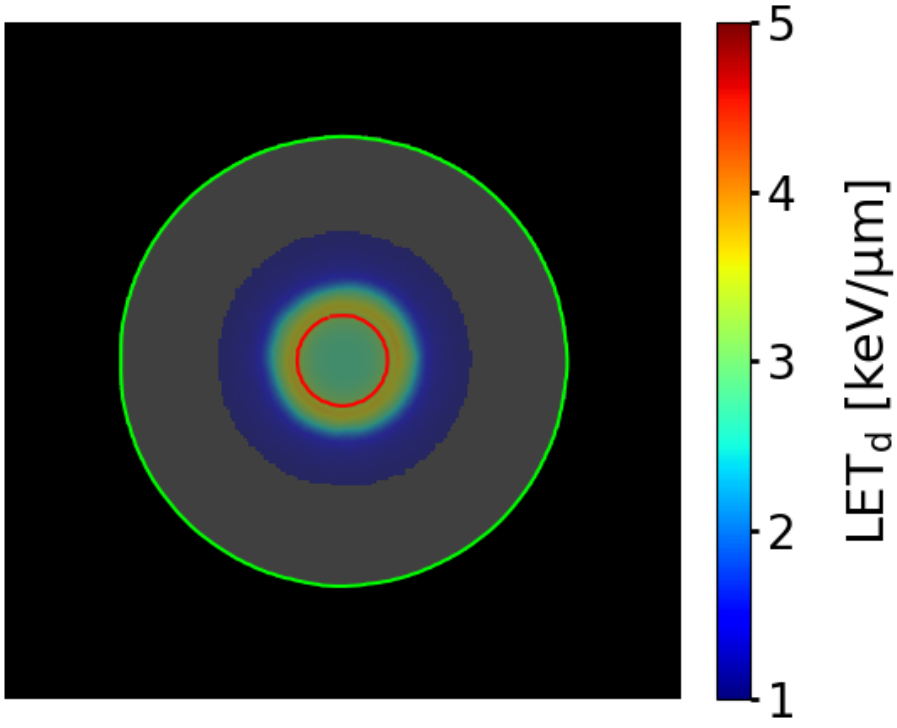

Figure 6.6: LET_d distribution for the water phantom 360^O arc case, for. The dose cutoff was set to 0.2Gy.

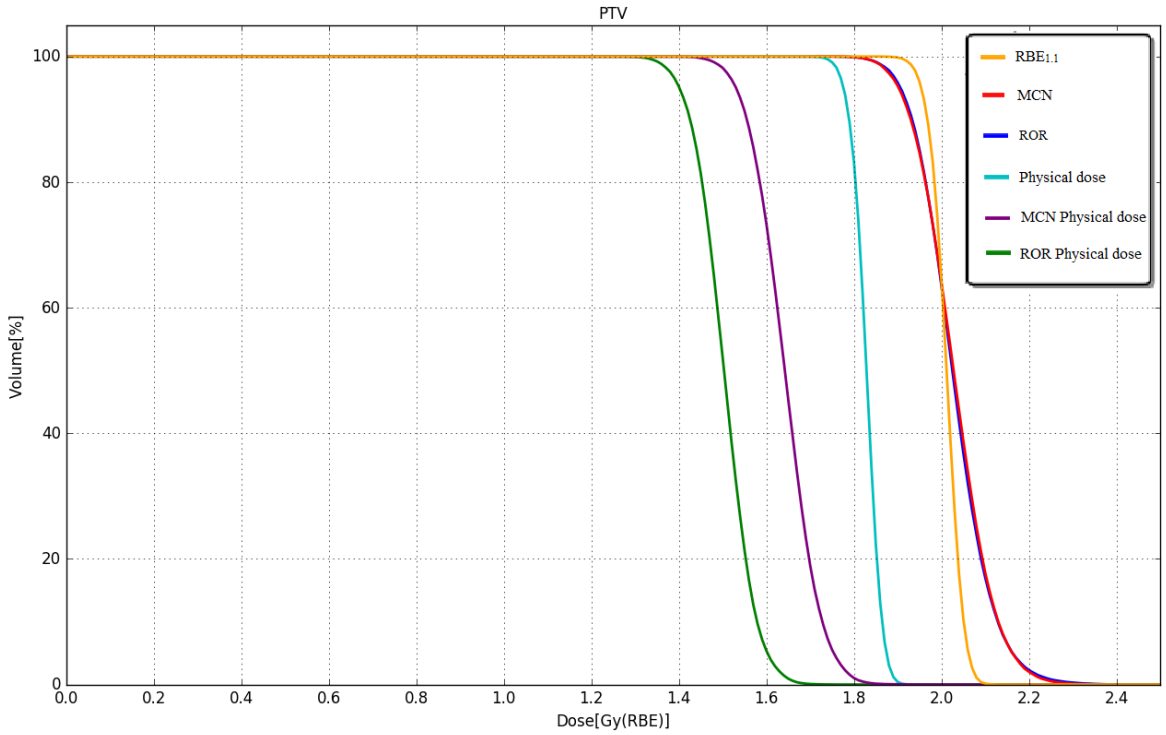

Figure 6.7: DVHs of the water phantom case with 2 opposing fields for the $RBE_{1.1}$, MCN, RORU models and corresponding physical doses for each model.

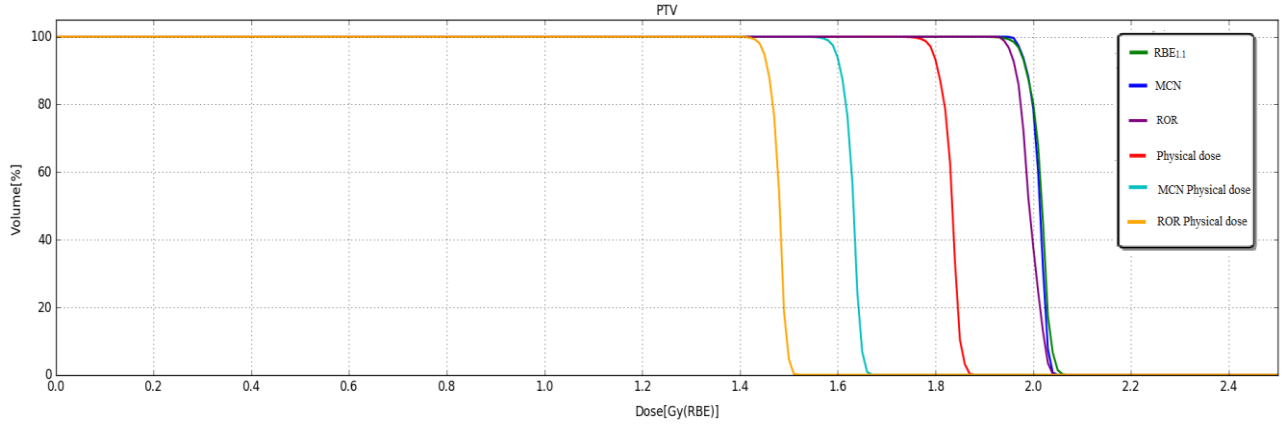

Figure 6.8: DVHs of the water phantom case with the 360^{O} arc plan for the $RBE_{1.1}$, MCN, RORU models and corresponding physical doses for each model.

Table 6.1: Dose metrics for the PTV in the water phantom case with two opposing fields (top) and the 360^{O} arc (bottom). Metrics are reported for each of the biological models. The corresponding physical doses for each model are given in parenthesis. $D_{95\%}$ and $D_{2\%}$ represent the dose delivered to 95% and 2% of the volume of the PTV respectively.

Model	**Mean dose [Gy(RBE)]**	**$D_{95\%}$[Gy(RBE)]**	**$D_{2\%}$[Gy(RBE)]**
	Opposing fields		
$RBE_{1.1}$	2.01 (1.83)	1.95 (1.78)	2.07 (1.89)
MCN	2.03 (1.64)	1.90 (1.53)	2.20 (1.78)
RORU	2.03 (1.50)	1.91 (1.40)	2.21 (1.63)
	360^{O} arc		
$RBE_{1.1}$	2.01 (1.83)	1.98 (1.8)	2.05 (1.86)
MCN	2.01 (1.63)	1.98 (1.60)	2.04 (1.66)
RORU	1.99 (1.48)	1.95 (1.45)	2.03 (1.51)

Table 6.2: RBE metrics for the PTV in the water phantom case with two opposing fields (top) and the 360^{O} arc (bottom). Metrics are reported for each of the variable RBE models.

Model	**Mean RBE**	**Min RBE**	**Max RBE**
		Opposing fields	
MCN	1.23	1.19	1.33
RORU	1.35	1.27	1.52
		360^{O} arc	
MCN	1.23	1.22	1.26
RORU	1.35	1.32	1.40

Table 6.3: LETd metrics for the PTV in the water phantom case with two opposing fields (top) and the 360^{O} arc (bottom).

	Mean LET	**Min LET**	**Max LET**
		Opposing fields	
LETd [keV/μm]	2.99	2.50	4.07
		360^{O} arc	
LETd [keV/μm]	2.94	2.68	3.37

6.2 Patient plans

6.2.1 Patient plan - 2 opposing fields

Figure 6.9 shows the biological dose distribution for $RBE_{1.1}$ as well as the two variable RBE models used. All models give a reasonably homogenous dose of 54.0Gy(RBE). This is supported by both the DVH in Figure 6.15 and dose metrics in Table 6.4. The mean doses predicted by $RBE_{1.1,}$ MCN and RORU were 54.0Gy(RBE), 54.0Gy(RBE) and 53,8Gy(RBE) respectively, illustrating that the optimizer is able to create homogeneous dose with the prescribed dose to the PTV for all the models.

The DVH in Figure 6.15 shows that the dose profiles for all models are similar. For all models the difference between the mean dose and $D_{95\%}$ are within 2Gy(RBE) and the difference between the $D_{2\%}$ and the mean dose are within 3Gy(RBE). The DVH also shows physical dose profiles corresponding to each biological model. The mean physical doses for $RBE_{1.1}$, MCN and RORU are 49.1Gy(RBE), 44.3Gy(RBE) and 40.9Gy(RBE), respectively. This means that both variable models predict lower physical doses than $RBE_{1.1}$, as seen for both water phantom plans.

Figure 6.11 shows the RBE distributions for both variable RBE models, Figure 6.13 shows the LET_d distribution and Table 6.5 displays RBE metrics for the PTV for each variable RBE model. The mean RBE values predicted for the PTV were 1.22 and 1.31 for MCN and RORU respectively, which means that both variable models predict higher RBE-values for the PTV than $RBE_{1.1}$, as could also be concluded from the reduced physical dose for these models. The figures also show that high LET values correspond with high RBE values, and that both the highest RBE and LET values are found outside the PTV.

6.2.2 Patient plan - Two 120^{O} opposing arcs

Figure 6.10 shows the RBE weighted dose distributions for $RBE_{1.1}$, and the MCN and RORU models. All models predict a reasonably homogenous dose to the PTV of 54 Gy(RBE). This is supported by the DVH in Figure 6.16 and the dose metrics in Table 6.4. The mean dose predicted by $RBE_{1.1}$, MCN and RORU were 54.0 Gy(RBE), 54.2 Gy(RBE), and 54.1 Gy(RBE), respectively. This shows that the optimizer is able to create acceptable treatmeant plans using all the applied RBE models, delivering the prescribed homogeneous dose to the PTV. The deviation between the mean dose and both $D_{95\%}$ and $D_{2\%}$ are within 2Gy(RBE) for all models.

The DVH in Figure 6.16 also show physical doses corresponding to each biological model. The mean physical doses predicted by $RBE_{1.1}$, MCN and RORU were 49.1 Gy(RBE), 44.5 Gy(RBE), 41.2 Gy(RBE), respectively. Both variable RBE models predict lower physical dose to the PTV than $RBE_{1.1}$.

Figure 6.12 shows RBE distributions for the variable RBE models, Figure 6.14 shows a LET_d distribution, and Table 6.5 displays RBE metrics for the PTV for each variable RBE model. Both models predict RBE values above 1.1 for the entire PTV. The mean RBE predicted by MCN and RORU for the PTV were 1.22 and 1.31, respectively. The figures also show that high LET values correspond with high RBE values, and that both the highest RBE and LET values are found outside the PTV.

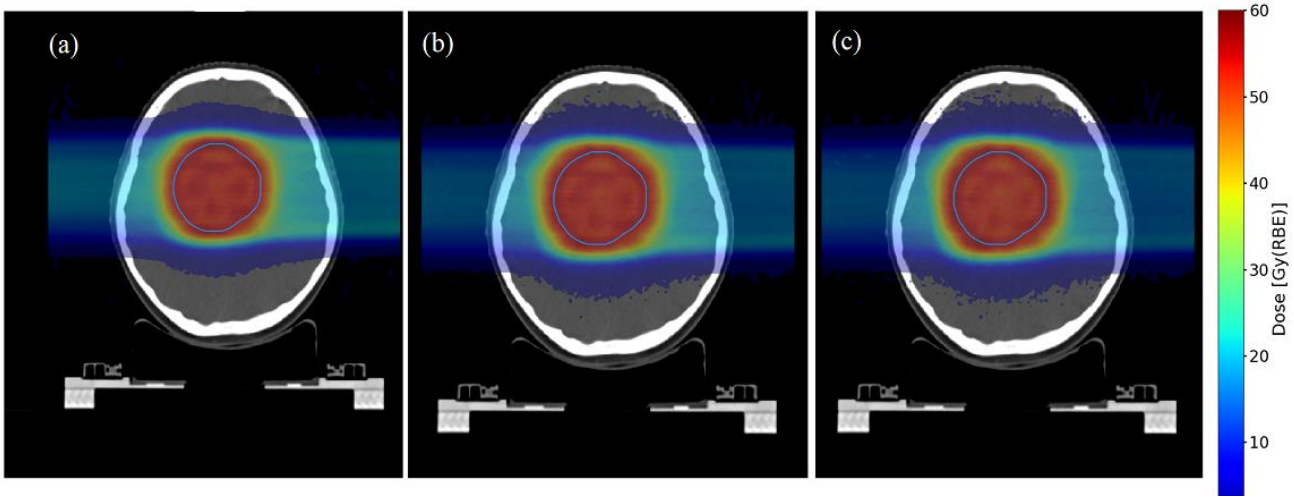

Figure 6.9: RBE weighted fraction dose distributions on a plane through the center of the PTV for the patient case with two opposing fields, for (a) $RBE_{1.1}$ and for the biological models (b) MCN and (c) RORU in a plane through the center of the PTV. The PTV is marked with a blue outline. The prescribed dose to the PTV is 54.0Gy.

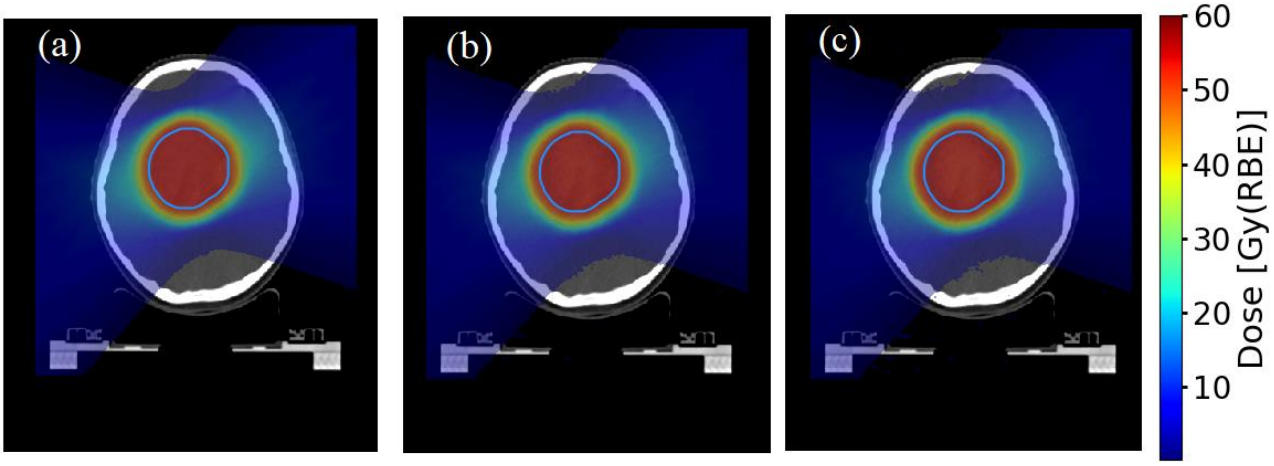

Figure 6.10: RBE weighted fraction dose distributions on a plane through the center of the PTV for the patient case with two opposite arcs, for (a) $RBE_{1.1}$, (b) MCN and (c) RORU. The blue outline marks the PTV. The prescribed dose to the PTV is 54.0Gy.

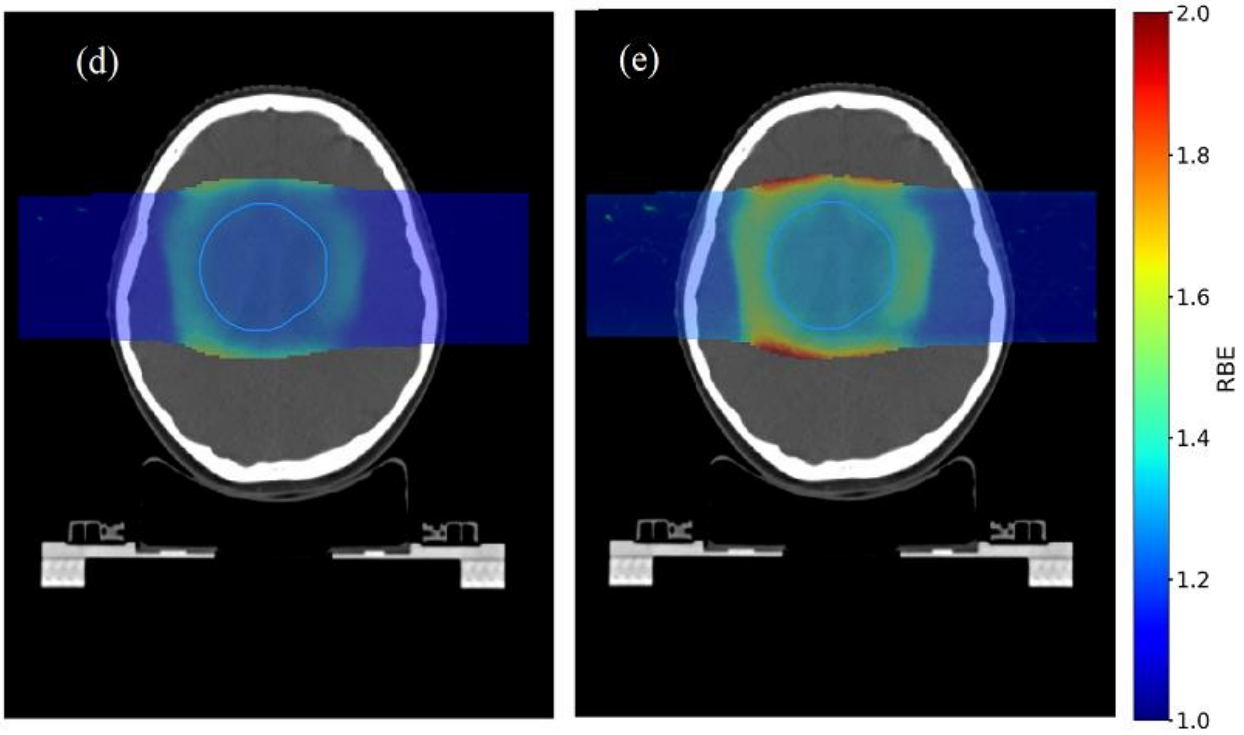

Figure 6.11: RBE distribution for the patient case with two opposing fields, for MCN (d) and RORU (e) and LET_d distribution (f). The dose cut-off was set to 5Gy.

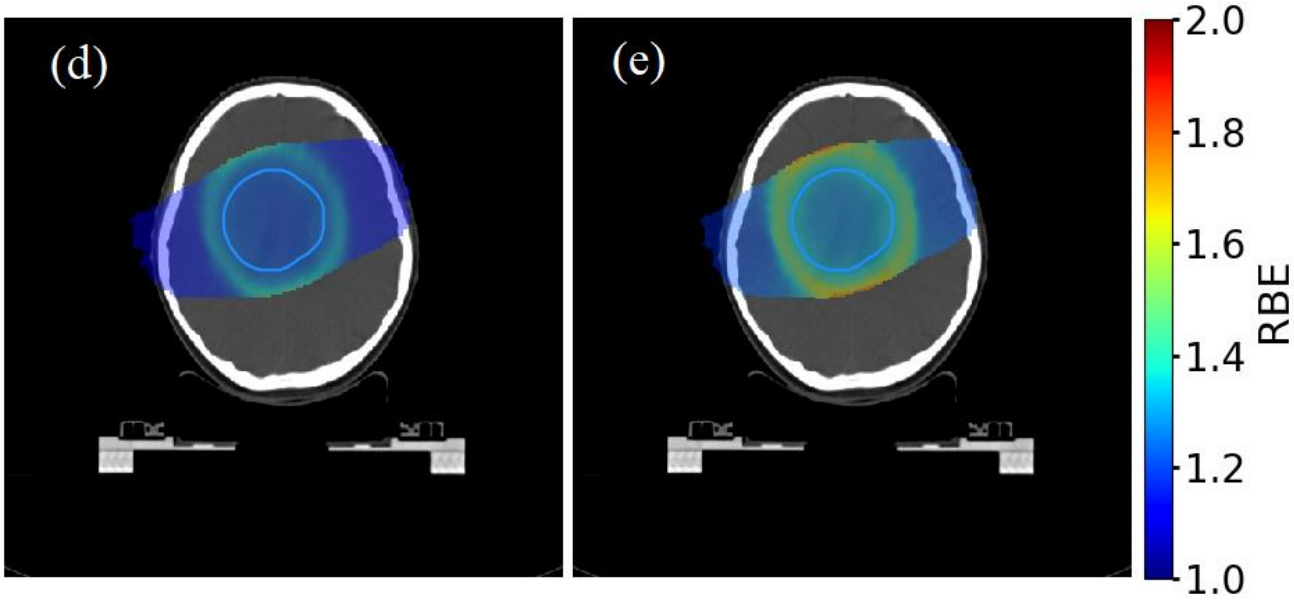

Figure 6.12: RBE distributions for the patient case with two opposite arcs, for (d) MCN and (e) RORU. The dose cut-off was set to 5Gy.

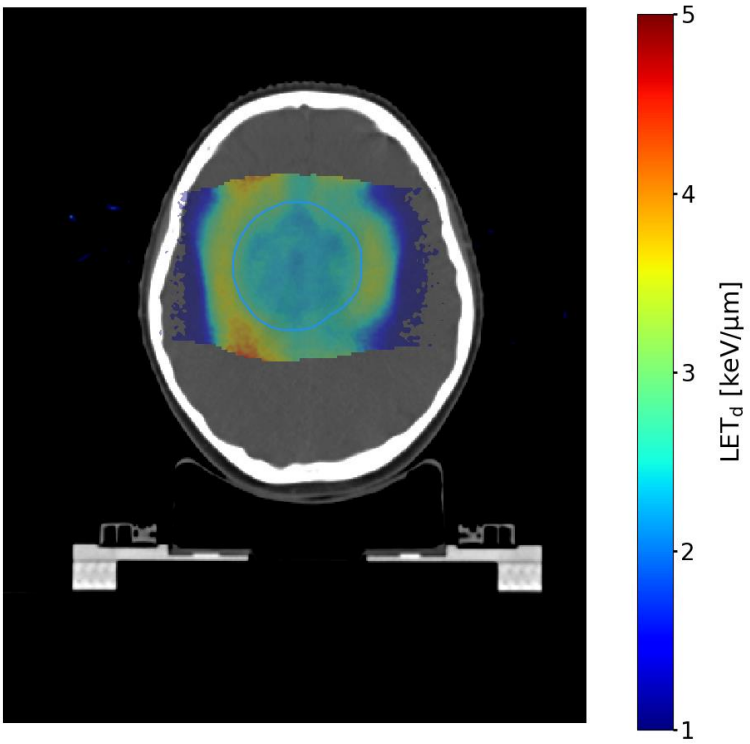

Figure 6.13: LET$_d$ distribution for the patient case with two opposing fields. The dose cutoff is was to 5Gy

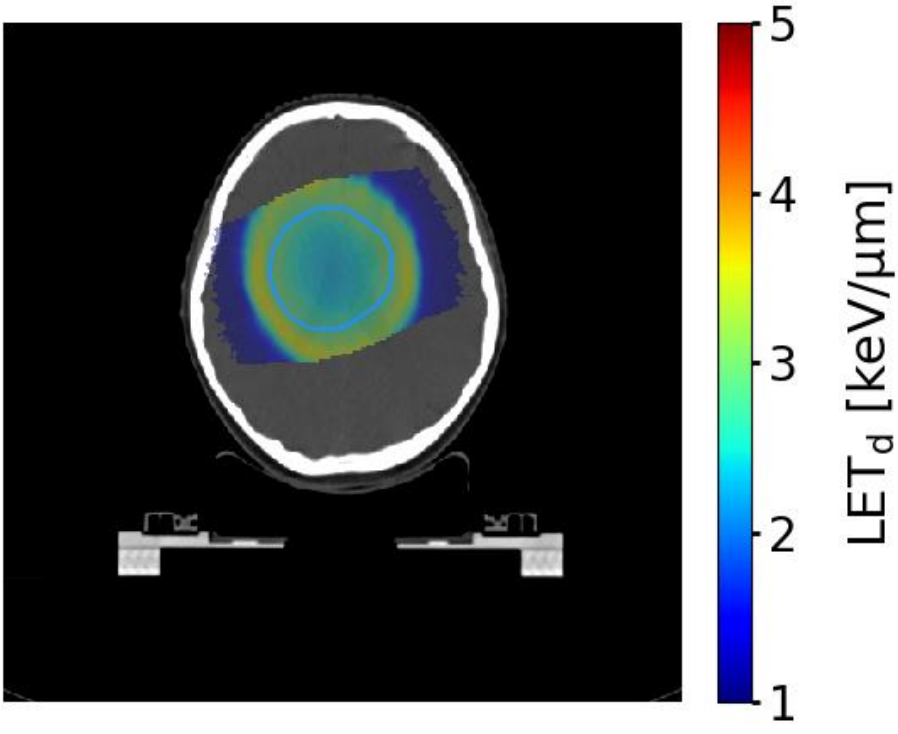

Figure 6.14: LET$_d$ distribution for the patient case with two opposite arcs. The dose cutoff was set to 5Gy

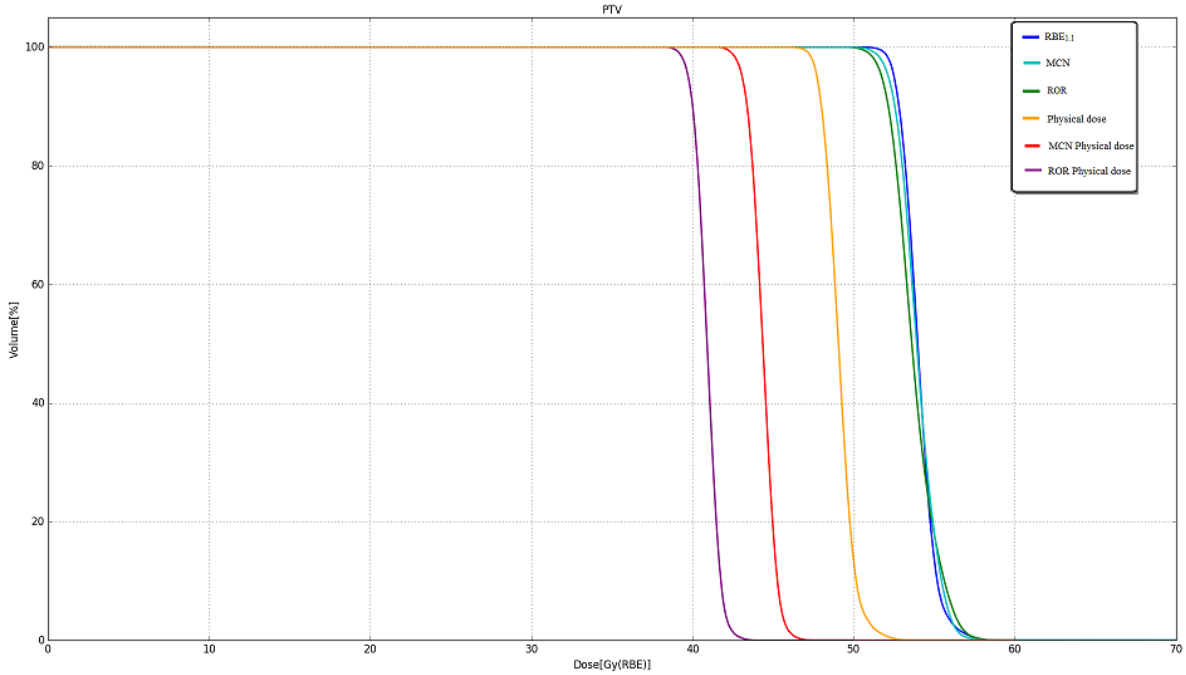

Figure 6.15: DVHs of the patient case with 2 opposing fields for the $RBE_{1.1}$, McNamara, Rorvik models and corresponding physical doses for each model.

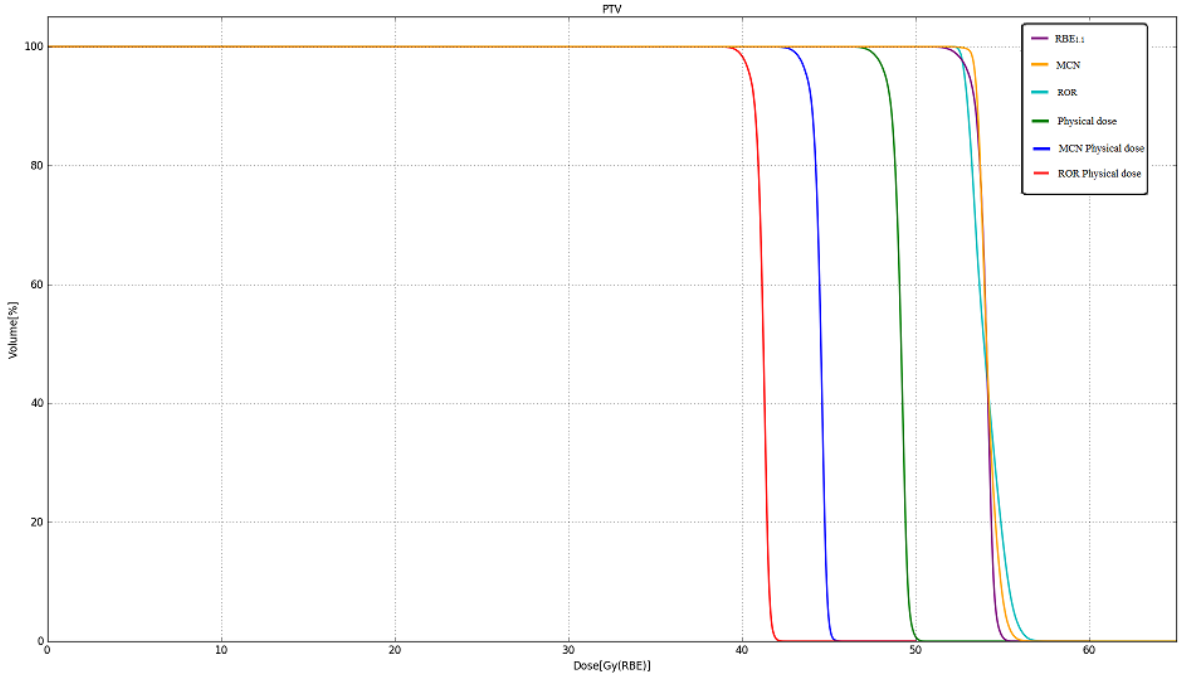

Figure 6.16: DVHs of the water phantom case with 2 opposing arcs for the $RBE_{1.1}$, McNamara, Rorvik models and corresponding physical doses for each model.

Table 6.4: Dose metrics for the PTV in the patient case with two opposing fields (top) and the two 120^O opposing arcs plan (bottom). Metrics are reported for of the each biological models. The corresponding physical doses for each model are given in parenthesis. $D_{95\%}$ and $D_{2\%}$ represent the dose delivered to 95% and 2% of the volume of the PTV respectively.

Model	**Mean dose [Gy(RBE)]**	**$D_{95\%}$[Gy(RBE)]**	**$D_{2\%}$[Gy(RBE)]**
	Opposing fields		
$RBE_{1.1}$	54.01 (49.09)	52.51 (47.72)	56.40 (51.26)
MCN	53.95 (44.34)	52.15 (43.08)	56.32 (45.87)
RORU	53.75 (40.90)	51.78 (39.73)	56.73 (42.35)
	Opposing 120^O arcs		
$RBE_{1.1}$	54.00 (49.09)	53.09 (48.27)	54.81 (49.83)
MCN	54.16 (44.48)	53.43 (43.73)	55.43 (45.07)
RORU	54.07 (41.17)	52.82 (40.47)	56.03 (41.76)

Table 6.5: RBE metrics for the PTV in the patient case with two opposing fields (top) and with two 120^{O} opposing arcs (bottom). Metrics are reported for each of the variable RBE models.

Model	Mean RBE	Min RBE	Max RBE
Opposing fields			
MCN	1.22	1.19	1.26
RORU	1.31	1.27	1.39
Opposing 120^{O} arcs			
MCN	1.22	1.21	1.24
RORU	1.31	1.28	1.36

Table 6.6: LETd metrics for the PTV in the patient case with two opposing fields (top) and with two 120^{O} opposing arcs (bottom).

	Mean LET	Min LET	Max LET
Opposing fields			
LETd [keV/μm]	2.50	2.16	3.55
Opposing 120^{O} arcs			
LETd [keV/μm]	2.62	2.21	3.29

6.3 360^{O} arc plan for the water phantom with lower maximum proton energy

Figure 6.17 shows the biological dose distributions for the 360^{O} arc water phantom arc plan, optimized for $RBE_{1.1}$. Therefore, the MCN and RORU models predict higher doses to the PTV than $RBE_{1.1}$. From the metrics in Table 6.7, the dose predicted by $RBE_{1.1}$, MCN and RORU were 1.99 Gy(RBE), 2.35 Gy(RBE) and 2.60 Gy(RBE), respectively.

The dose distribution, the dose metrics and the DVH in Figure 6.20, shows that the dose to the PTV is inhomogeneous compared to all previously presented treatment plans. For all biological the difference between the mean dose and $D_{95\%}$ are greater than 0.1Gy(RBE), and the difference between $D_{2\%}$ and the mean dose are greater than 0.25Gy. Both the optimization process in the TPS and the optimizer used provided inhomogeneous dose profiles for this plan.

Figure 6.18 and Figure 6.19 shows the RBE distributions for each model and a LET_d distribution for the 360^{O} arc water phantom arc plan. These figures show that the highest RBE and LET values are located inside the PTV. From Table 6.8 the mean RBE in the PTV for MCN and RORU were 1.29 and 1.43, respectively. These RBE values for the PTV are higher than for all other presented treatment plans. Table 6.9 displays LET_d metrics. The mean and max LET_d for the PTV are 4.32 [keV/μm] and 4.85 [keV/μm], respectively. These values are higher than for all other presented treatment plans. Similar to all other presented treatment plans, higher LET_d values correspond with higher RBE values.

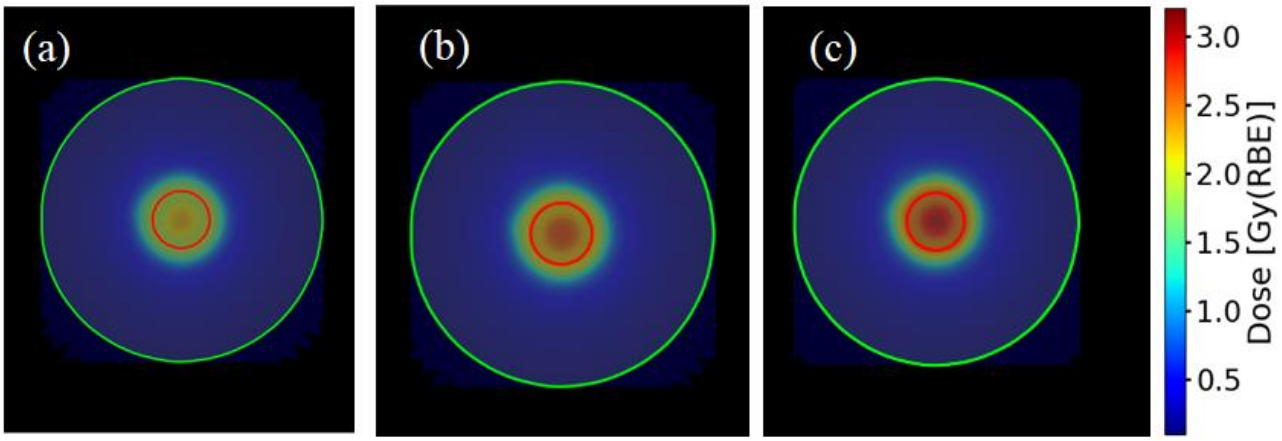

Figure 6.17: Dose distribution in a plane through the center of the PTV for (a) $RBE_{1.1}$, (b) MCN and (c) RORU. The red outline marks the PTV. The prescribed dose is 2.0Gy.

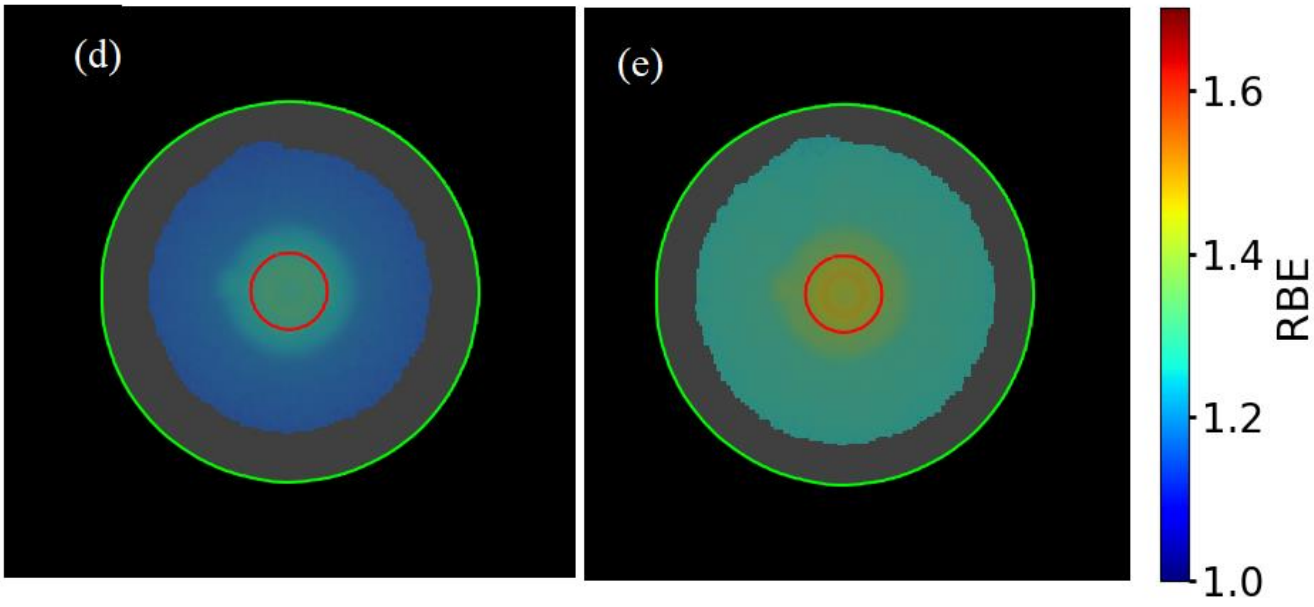

Figure 6.18: RBE distributions in a plane through the center of the PTV for (d) MCN and (e) RORU. The dose cut-off was set to 0.2Gy.

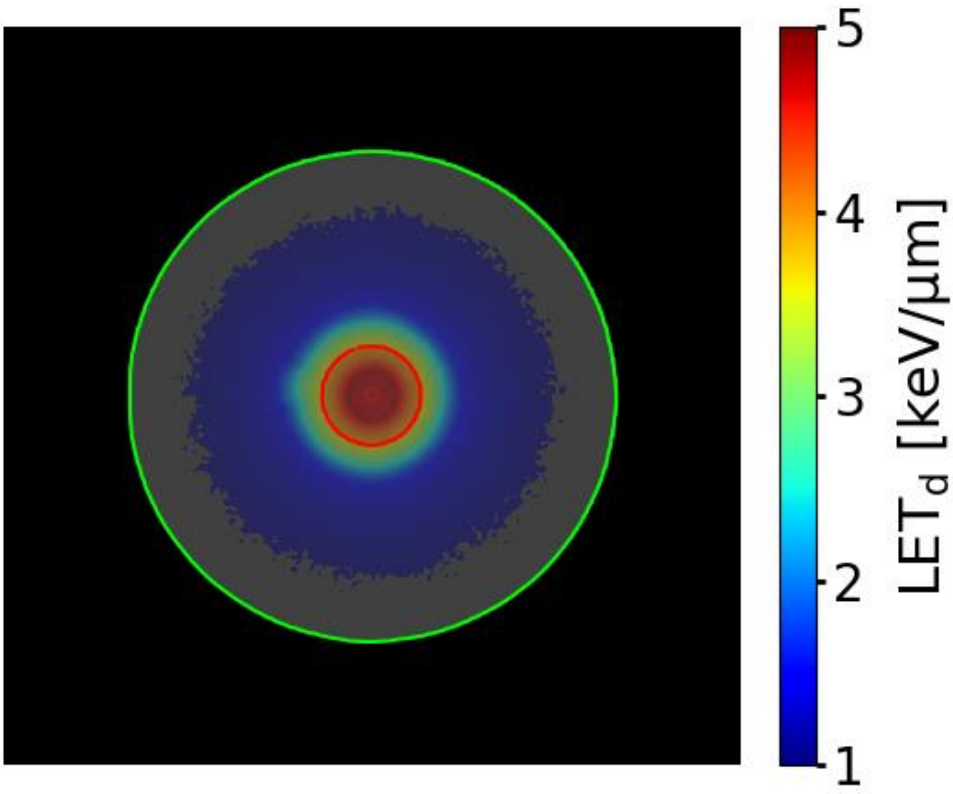

Figure 6.19: LET_d distribution. The dose cut-off was set to 0.2Gy

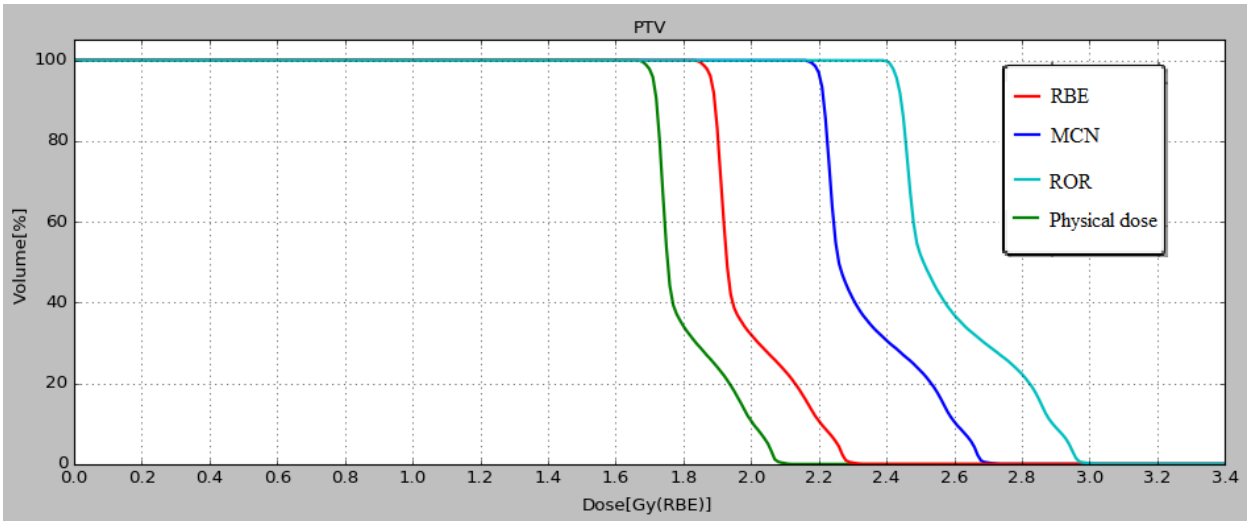

Figure 6.20: DVHs for the 360^O water phantom arc plan with reduced maximum proton energy.

Table 6.7: Dose metrics for the PTV in the 360^{O} water phantom arc case with lower maximum proton energy for each biological models. $D_{95\%}$ and $D_{2\%}$ represent the dose delivered to 95% and 2% of the volume of the PTV respectively.

Model	**Mean dose [Gy(RBE)]**	**$D_{95\%}$**	**$D_{2\%}$**
$RBE_{1.1}$	1.99	1.88	2.27
MCN	2.35	2.21	2.67
RORU	2.60	2.43	2.96

Table 6.8: RBE metrics for the PTV in the 360^{O} water phantom arc case with lower maximum proton energy for each variable RBE model.

Model	**Mean RBE**	**Min RBE**	**Max RBE**
MCN	1.29	1.26	1.31
RORU	1.43	1.38	1.47

Table 6.9: LETd values for the PTV in the 360^{O} water phantom arc case with reduced maximum proton energy

	Mean LET	**Min LET**	**Max LET**
LETd [keV/μm]	4.32	3.64	4.85

7. Discussion

In this project, a prototype optimizer has been used together with the FLUKA MC-code to re-optimize IMPT and PAT treatment plans with respect to different RBE-models. In addition, a treatment plan with lower maximum proton energy was produced, as an attempt to shift the highest RBE values in to the PTV. The dose, RBE and LET distributions of each plan have been presented. The results indicate that the PTV achieved the prescribed dose of 2.0Gy(RBE) for the water phantom plans and 54.0Gy(RBE) for the patient plans, although the PTV in the water phantom plan with lower maximum energy received inhomogeneous dose. However, the water phantom case with lower maximum energy showed promising results in terms of placing the highest RBE and LET_d values inside the PTV.

7.1 PAT and IMPT comparison

Compared to the 2 fields plan the arc plans show promising results for both the water phantom case and the patient case. For both cases the doses of the arc plans to the PTV were more homogenous than for the 2 fields plans, for $RBE_{1.1}$, MCN and RORU. The homogeneity of the RBE and LET values inside the PTV were also greater for both arc plans than respective 2 fields plans. The differences in dose homogeneity are largest for the RORU and MCN weigthed dose distributions for the water phantom and patient cases. The water phantom plans. For this case the arc plan reduced the spread of the MCN and RORU weigthed dose distribution by more than 50%. However, the dose homogeneity of the water phantom 2 fields case is significantly poorer than for the water phantom arc case and the patient case. A possible explanation for this, is that the 2 fields water phantom plan used significantly pencil beam spots, with larger spacing between each spot, than the three other cases. This might have an impact on the optimization process, as it could be easier for the optimizer to optimize plans with more beam spots inside the optimization volume.

The arc plans also improved dose gradients, and reduced the areas receiving intermediate dose levels compared to the 2 fields plans, in both the phantom and patient cases. However, in the arc plans a larger area received low dose. Delivering low dose to large areas in patients might result in higher risks of secondary cancer. Toussaint, et al. [54] suggests that possible implication of large low dose areas on secondary cancer risk should be studied further.

7.2 RBE model dose difference

For the four treatment plans that were optimized with respect to the MCN and RORU models, both the MCN and RORU models provided lower physical doses than $RBE_{1.1}$, and the RORU model provided the lowest physical dose of the two variable models. The RORU model provided physical dose to the PTV, which was generally 19% lower than the physical dose provided from $RBE_{1.1}$, while the MCN model was generally 10% lower. For the four treatment plans the mean RBE values for the PTV provided from the RORU model were 7-9% higher than the mean RBE values provided by MCN. The considerable difference between the RBE and RBE-weighted doses for RORU and MCN are similar to results produced by Rørvik et al. [53].

The RBE and physical dose difference between the RORU and MCN models are not homogeneous and increase with increasing RBE-values. The RBE max values provided by RORU were 10-13% higher than the values provided by MCN. This leads to the physical doses being inhomogeneous, and the largest dose differences between RORU and MCN are found towards the distal end of the beams, where the highest RBE values are found.

Overall, the results indicate that using RBE-models in the plan optimization process can result in lower physical dose, decreasing the risk of side effects, while delivering the prescribed biological dose to the target volume. However, the considerable variations between the different RBE models gives rise to uncertainty when applying RBE-models for clinical treatment planning. This uncertainty might lead to under dosage of the target volume, reducing the probability of successful treatment. For this reason, variable RBE-models should at the moment not be implemented in clinical treatment planning. This is supported by Paganetti et al. [55], suggesting that the clinical RBE of 1.1 is sufficient for now. Therefore, more research should be done in the field of RBE models to make the implementation of a variable RBE clinically possible, as using a variable RBE model in treatment planning has the potential to reduce physical dose delivered significantly.

7.3 The 360^{O} water phantom arc plan with lower maximum proton energy

The 360^{O} water phantom arc plan with lower maximum proton energy showed promising results in placing the highest RBE and LET inside the PTV. However, the dose distributions for all biological models were inhomogeneous, delivering significantly higher dose to the center of the PTV than the edges. Both the TPS and the prototype optimizer provided inhomogeneous dose distribution for the plan. One of the possible explanations for the inhomogeneity is the way the plan was constructed in the TPS. The plan was constructed by removing the highest energy proton beam spots for each beam of the 360^{O} water phantom arc plan. This is not ideal, and a method for constructing plans with lower-than-normal max proton energy should be developed. Another possible explanation for the inhomogeneous dose provided by the TPS and the optimizer is the high amount of pencil beams used in this plan. The size of the .dat file containing information about the pencil beams caused the optimizer to shut down when running biological optimizations of the plan. The high amount of pencil beam might also have cause problems for the optimization process in the TPS.

The concept of placing the highest RBE and LET_d values inside the target volume should be explored further, as the higher RBE inside the target will result in a reduction of physical dose needed for tumor control. This could also reduce side effects, as the high LET from the distal part of proton beams is a major concern for normal tissue damage in proton therapy.

8. Conclusion

In this project proton arc therapy was explored. By using a combination of a commercial treatment planning system, custom made code, simulation code and a prototype dose optimizer, the dose, RBE and LET distributions from proton arc plans were studied and compared to IMPT plans.

The results in this thesis show that proton arc therapy has the potential to increase dose homogeneity and improve dose gradients. The largest increases in dose homogeneity were seen for the variable RBE-weigthed doses. In addition, the results showed that the physical dose from the RBE-weighted models was reduced by 7 to 13% compared to $RBE_{1.1.}$ This result points out the importance of biological treatment optimization, as it has the potential to reduce physical dose without comprising tumor control.

The results from the 360^{O} water phantom arc plan with lower maximum proton energy, illustrates the possibility of placing the highest RBE and LET_d values inside the target volume. However, the dose distributions for this plan were inhomogeneous, further development of this is needed, as it can result reduction of physical dose needed for tumor control.

9. References

1. Kreftregisteret.no. *Kreft i Norge*. 2021 19.02.2021; Available from: https://www.kreftregisteret.no/Registrene/Kreft_i_Norge/.
2. Bergen, H. *Innføring av protonbehandling til Norge*. 2020 21.09.2020; Available from: https://helse-bergen.no/om-oss/protonsenter-i-bergen/innforing-av-protonbehandling-til-norge.
3. Slater, J.M., *From X-Rays to Ion Beams: A Short History of Radiation Therapy*, in *Biological and Medical Physics, Biomedical Engineering*, U. Linz, Editor. 2011, Springer.
4. Karzmark, C.J. and N.C. Pering, *Electron linear accelerators for radiation therapy: history, principles and contemporary developments.* Phys Med Biol, 1973. **18**(3).
5. Wilson, R.R., *Radiological Use of Fast Protons.* Radiology, 1946. **47**(5): p. 487-491.
6. M.L.M. Boone, J.H.L., W.G. Connor, et al., *Introduction to the use of protons and heavy ions in radiation therapy: historical perspective.* International journal of radiation oncology, biology, physics., 1977(3): p. 65-69.
7. U. Amaldi, G.K., *Radiotherapy with beams of carbon ions.* Report on progresss in physics, 2005(68): p. 1861-1882.
8. Paganetti, H., *Proton Beam Therapy*. 2017.
9. Mohan, R. and D. Grosshans, *Proton therapy - Present and future.* Adv Drug Deliv Rev, 2017. **109**: p. 26-44.
10. Hong, T.S., et al., *Intensity-modulated radiation therapy: emerging cancer treatment technology.* Br J Cancer, 2005. **92**(10): p. 1819-24.
11. Girdhani, S., R. Sachs, and L. Hlatky, *Biological effects of proton radiation: what we know and don't know.* Radiat Res, 2013. **179**(3): p. 257-72.
12. Quan, E.M., et al., *A comprehensive comparison of IMRT and VMAT plan quality for prostate cancer treatment.* Int J Radiat Oncol Biol Phys, 2012. **83**(4): p. 1169-78.
13. Ding, X., et al., *Spot-Scanning Proton Arc (SPArc) Therapy: The First Robust and Delivery-Efficient Spot-Scanning Proton Arc Therapy.* Int J Radiat Oncol Biol Phys, 2016. **96**(5): p. 1107-1116.
14. Li, X., et al., *The first prototype of spot-scanning proton arc treatment delivery.* Radiother Oncol, 2019. **137**: p. 130-136.
15. Toussaint, L., et al., *Towards proton arc therapy: physical and biologically equivalent doses with increasing number of beams in pediatric brain irradiation.* Acta Oncol, 2019. **58**(10): p. 1451-1456.
16. Seco, J., et al., *Proton arc reduces range uncertainty effects and improves conformality compared with photon volumetric modulated arc therapy in stereotactic body radiation therapy for non-small cell lung cancer.* Int J Radiat Oncol Biol Phys, 2013. **87**(1): p. 188-94.
17. Freeman, T. *Proton arc therapy: the next evolution in proton delivery?* 2019; Available from: https://physicsworld.com/a/proton-arc-therapy-the-next-evolution-in-proton-delivery/.
18. Joiner, M. and A.v.d. Kogel, *Basic Clinical Radiobiology*. 4th ed. 2009.
19. Durante, M., *New challenges in high-energy particle radiobiology.* Br J Radiol, 2014. **87**(1035).

20. Polster, L., et al., *Extension of TOPAS for the simulation of proton radiation effects considering molecular and cellular endpoints.* Phys Med Biol, 2015. **60**(13): p. 5053-70.
21. Newhauser, W.D. and R. Zhang, *The physics of proton therapy.* Phys Med Biol, 2015. **60**(8): p. R155-209.
22. Henley, E., M., & Garcia, A., *Passage of Radiation Through Matter*, in *Subatomic Physics*. 2012, World Scientific. p. 39-52.
23. Bethe, H., *Zur theorie des durchgangs schneller korpuskularstrahlen durch materie*, in *Annalen der Physik*. 1930. p. 325-400.
24. Ytre-Hauge, K.S., *Measurements and Monte Carlo Simulations of Neutron Doses from Radiation Therapy with Photons, Protons and Carbon Ions*. 2013.
25. Kaderka, R., et al., *Out-of-field dose measurements in a water phantom using different radiotherapy modalities.* Phys Med Biol, 2012. **57**(16): p. 5059-74.
26. ICRP, *The 2007 Recommendations of the International Commission on Radiological Protection. ICRP publication 103.* Ann ICRP, 2007. **37**(2-4): p. 1-332.
27. Paganetti, H., *Proton therapy physics*. 2012: CRC Press - Taylor & Francis Group.
28. Landberg, T., et al., *Report 50.* Journal of the International Commission on Radiation Units and Measurements, 1993. **os26**(1).
29. Zirkle, R.E., D.F. Marchbank, and K.D. Kuck, *Exponential and sigmoid survival curves resulting from alpha and x irradiation of Aspergillus spores.* J Cell Physiol Suppl, 1952. **39**(Suppl. 1): p. 78-85.
30. Baskar, R., et al., *Cancer and radiation therapy: current advances and future directions.* Int J Med Sci, 2012. **9**(3): p. 193-9.
31. Fjæra, L.F., *Development of a Monte Carlo Based Treatment Planning Verification Tool for Pariticle Therapy*, in *Department of Physics and Technology* 2016, University of Bergen.
32. Guan, F., et al., *Analysis of the track- and dose-averaged LET and LET spectra in proton therapy using the geant4 Monte Carlo code.* Medical Physics, 2015. **42**(11): p. 6234-6247.
33. Hall, E.J., and A. J. Giaccia, *Radiobiology for the Radiologist*. 6th ed. 2006: Lippincott Williams & Wilkins.
34. ICRU, *ICRU report no 78: Prescribing, recording and reporting proton beam therapy.* 2007.
35. R. G. Dale, B.J., *The assessment of RBE effects using the concept of biologically effective dose.* Int. J Radiat. Oncol,, 1999. **43**: p. 639-645.
36. Rørvik, E., et al., *A phenomenological biological dose model for proton therapy based on linear energy transfer spectra.* Medical Physics, 2017. **44**(6): p. 2586-2594.
37. Holthusen, H., *Erfahrungen über die Verträglichkeitsgrenze für Röntgenstrahlung und deren Nutzanwendung zur Verhütung von Schäden.* Strahlenther. Onkol., 1936. **57**: p. 30-36.
38. Smith, N., and Webb, A., *Introduction to Medical Imaging: Physics Engineering and Clinical Applications.* 2010, Cambridge: Cambridge University Press.
39. De Marzi, L., et al., *Treatment Planning Systems and Hadron Therapy Practice in France.* 2017: p. 467-494.
40. Gu, W., et al., *A novel energy layer optimization framework for spot-scanning proton arc therapy.* Med Phys, 2020. **47**(5): p. 2072-2084.

41. Flynn, R.T., et al., *Comparison of intensity modulated x-ray therapy and intensity modulated proton therapy for selective subvolume boosting: a phantom study.* Phys Med Biol, 2007. **52**(20): p. 6073-91.
42. Blanco Kiely, J.P. and B.M. White, *Dosimetric feasibility of single-energy proton modulated arc therapy for treatment of chordoma at the skull base.* Acta Oncol, 2016. **55**(9-10): p. 1243-1245.
43. Li, X., et al., *Improve dosimetric outcome in stage III non-small-cell lung cancer treatment using spot-scanning proton arc (SPArc) therapy.* Radiat Oncol, 2018. **13**(1): p. 35.
44. Ding, X., et al., *Have we reached proton beam therapy dosimetric limitations? - A novel robust, delivery-efficent and continuous spot-scanning proton arc (SPArc) therapy is to improve dosimetric outcome in treating prostate cancer.* Acta Oncol., 2018. **57**(3): p. 435-437.
45. Ding, X., et al., *Improving dosimetric outcome for hippocampus and cochlea sparing whole brain radiotherapy using spot-scanning proton arc therapy.* Acta Oncol, 2019. **58**(4): p. 483-490.
46. Jiang, H. and H. Paganetti, *Adaptation of GEANT4 to Monte Carlo dose calculations based on CT data.* Medical Physics, 2004. **31**(10): p. 2811.
47. Ferrari, A., et al., *FLUKA: A multi-particle transport code*, in *CERN-2005-10 (2005), INFN/TC_05/11, SLAC-R-773*. 2005.
48. Bohlen, T.T., et al., *The FLUKA Code: Developments and Challenges for High Energy and Medical Applications.* Nuclear Data Sheets, 2014. **120**: p. 211-214.
49. Battistoni, G., et al., *The FLUKA Code: An Accurate Simulation Tool for Particle Therapy.* Front Oncol, 2016. **6**: p. 116.
50. Vlachoudis, V. *FLAIR: A powerful but user friendly graphical interface for FLUKA.* in *International Conference on Mathematics, Computational Methods & Reactor Physics (M&C 2009)*. 2009. Saratoga Springs, New York.
51. W. Scneider, T.B., W. Schegel, *Correlation between CT numbers and tissue parameters needed for Monte Carlo simulations of clinical dose distributions.* Phys Med Biol, 2000. **45**(2).
52. McNamara, A.L., J. Schuemann, and H. Paganetti, *A phenomenological relative biological effectiveness (RBE) model for proton therapy based on all published in vitro cell survival data.* Phys Med Biol, 2015. **60**(21): p. 399-416.
53. Rorvik, E., et al., *Exploration and application of phenomenological RBE models for proton therapy.* Phys Med Biol, 2018. **63**(18): p. 185013.
54. L Toussaint, D.I., K S Holgersen, J B B Petersen, C H Stokkevåg, Y Lassen-Ramshad, O Casares-Magaz, A Vestergaard, L P Muren, *Towards proton arc therapy: Physical and biologically effective doses with increasing number of beams in pediatric brain irradiation.* In Review, Acta Oncol, 2019.
55. Paganetti, H., *Relative biological effectiveness (RBE) values for proton beam therapy. Variations as a function of biological endpoint, dose, and linear energy transfer.* Phys Med Biol, 2014. **59**(22): p. R419-72.

Appendix A Tables containing descriptions of steps in the method

Table A.1, Table A.2 and Table A.3 contain descriptions of the steps in the method.

Table A.1: Information about files and scripts used for initial FLUKA simulations

Script/file	Description
Treatment plan from the TPS	Contains CT-images, and information about pencil beam, ROIs and dose. Exported from the TPS in the DICOM-format
Sort_dicom.py	Converts information from the DICOM-files into input files for FLUKA
Source.f	Contains information about beam source
Input file	Input file for FLUKA
Fluscw.f	Contains information about beam weightings
Voxel file	Contains Information about the voxels in the phantom or patient, generated by FLUKA using CT images and data about materials
Pencil beam information (datfile)	Information about the different parameters for each pencil beam

Table A.2: Information about files and scripts used for the optimization process, as well as FLUKA dose verification

Script/file	**Description**
Create_files_for_optimizer.py	Generates files needed to run the optimizer
HU_changer.py	Reads in DICOM files and generates information about chosen ROIs
ROI and PTV information	Dose information and information about constraits for each ROI, generated by HU_changer.py
Optimizer	C++ based optimizer, described in 5.1.3
Reoptimized pencil beam information	Information generated by the optimizer about the new weightings for each pencil beam
make_reopt_datfile.py	Generates a .dat file containing the new weightings for each pencil beam from the optimizer
FLUKA simulation with reoptimized data.	New simulation run in FLUKA using the .dat file created by the make_reopt_datfile.py script.

Table A.3: Information about scripts and files used for extracting dose metrics and plotting dose data.

Script/file	**Description**
convert_to_dicom.py	Converts files generated from the FLUKA simulations into DICOM files
3D Slicer	Software program used to plot DVHs and display dose metrics
plot_dicom.py	Plots 2D dose distributions for a chosen DICOM file and CT slice.
2D Plots	2D dose results generated by plot_dicom.py
DVH	Dose Volume Histograms generated by Slicer, and by python scripts for plotting DVHs